Master Thesis

FH AACHEN
UNIVERSITY OF APPLIED SCIENCES

Development of the geometry and inclination measurement-system for an ice-borehole-logger

Matthias Hüther
17th February 2015
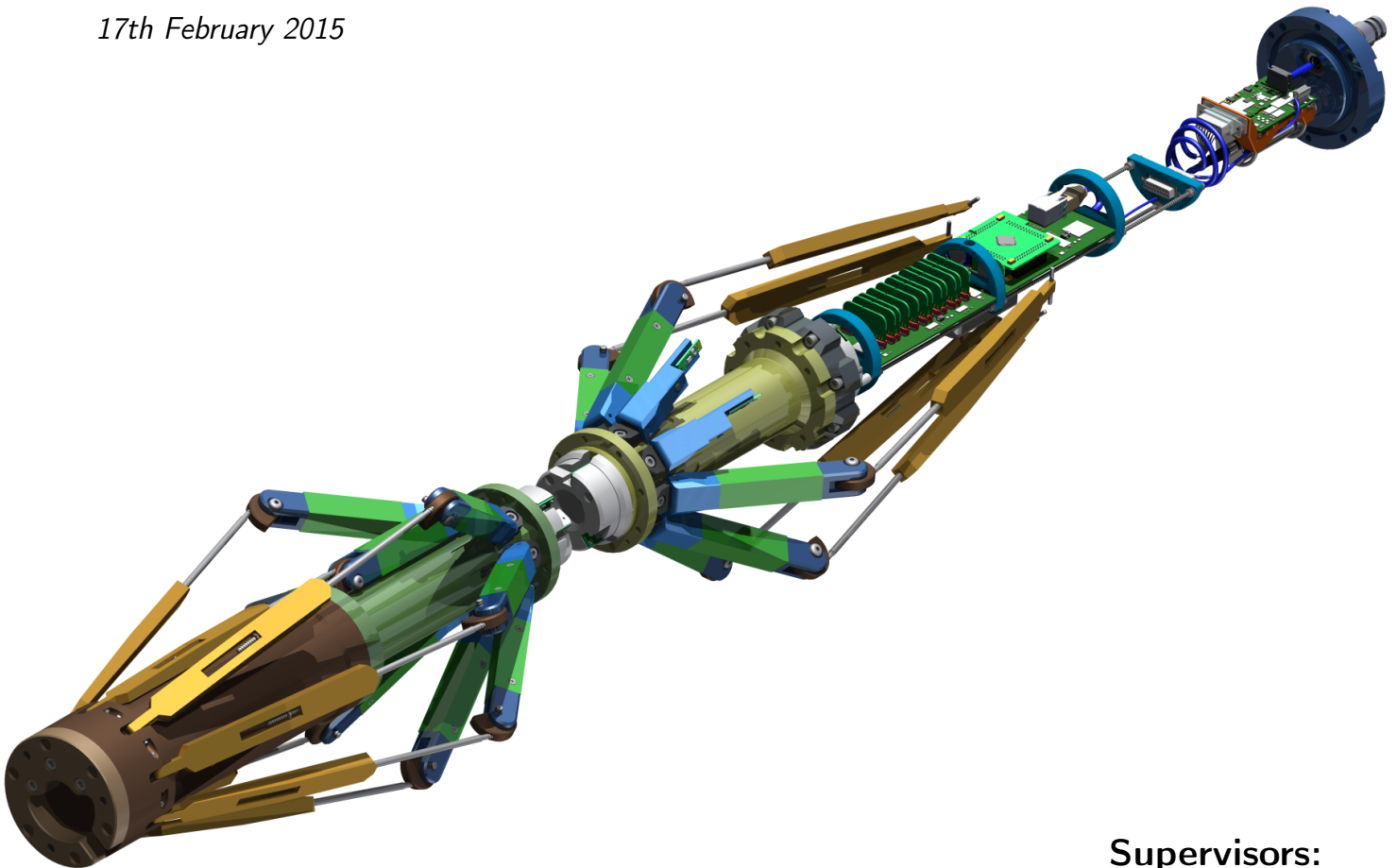
Supervisors:

Prof. Dr. Frank Wilhelms

Alfred-Wegener-Institut

Helmholtz-Zentrum für Polar- und Meeresforschung

Geowissenschaftliches Zentrum,
Georg-August-Universität Göttingen

Prof. Dr. Bernd Dachwald

FH Aachen

Erklärung

Ich versichere hiermit, dass ich die vorliegende Arbeit selbständig verfasst und keine anderen als die im Literaturverzeichnis angegebenen Quellen benutzt habe.

Stellen, die wörtlich oder sinngemäß aus veröffentlichten oder noch nicht veröffentlichten Quellen entnommen sind, sind als solche kenntlich gemacht.

Die Zeichnungen oder Abbildungen in dieser Arbeit sind von mir selbst erstellt worden oder mit einem entsprechenden Quellennachweis versehen.

Diese Arbeit ist in gleicher oder ähnlicher Form noch bei keiner anderen Prüfungsbehörde eingereicht worden.

Aachen, den 17. Februar 2015

_____

(Hüther, Matthias)

Abstract

This thesis presents the design of the hard- and software of a new shape measurement probe for ice boreholes. It allows logging the borehole's shape and its evolution in time, which relates to the local deformation regime in the borehole's vicinity. Therefore, the enhanced geometrical data contribute to the understanding of ice-sheet dynamics especially as a reference when verifying numerical simulations. The presented probe is designed to measure 16 individual points over the borehole circumference with three axial acceleration sensors based on micro-electro-mechanical systems (MEMS) design and the borehole inclination. This geometry data combined with the additional parameters pressure, density and temperature should be logged in boreholes filled with drill fluids over a maximum depth of 3.5 km in Greenland and Antarctica.

Zusammenfassung

Diese Arbeit beschreibt die Entwicklung einer Messelektronik inklusive zugehöriger Auswertesoftware einer Eisbohrlochgeometrie und -inklination vermessenden Sonde. Zweck eines solchen Messgerätes ist es, die im Zuge von Eiskernbohrungen entstandenen, Bohrlöcher in regelmäßigen Intervallen zu vermessen und Veränderungen der Ausrichtung und Form zu registrieren. Diese, durch das Fließen der Gletscher entstandenen, Veränderungen erlauben es Rückschlüsse über deren internen Zustand zu ziehen.

Die kombinierte Messung der Form und Ausrichtung konnte bisher nur in kurzen Bohrlöchern durchgeführt werden. Mithilfe der in dieser Arbeit beschriebenen Neuentwicklung des Alfred-Wegener-Institut Helmholtz-Zentrum für Polar- und Meeresforschung können nun mit Flüssigkeit gefüllte Tiefbohrlöcher (bis 3,5 km) in Grönland und der Antarktis vermessen werden.

Das eingesetzte Messprinzip der Geometriemessung beruht auf 16 Messarmen, die gleichmäßig über den Umfang verteilt eine Punktwolke erzeugen. Die dazu notwendige Winkelmessung wird genau wie die Messung der Ausrichtung über dreiachsige Beschleunigungssensoren durchgeführt, die auf einem mikroelektromechanischen Systems beruhen. Die Messungen können durch die zusätzlich aufgenommenen Parameter Druck und Dichte ergänzt werden. Zudem besitzt die Sonde eine Erweiterungsmöglichkeit für eine Temperaturmessung, sowie einen frei verfügbaren Ethernet Anschluss für zukünftige Ausbaustufen.

Contents

1. Introduction

This thesis covers the design phase of a probe, measuring the shape and the inclination of boreholes in glaciers. This investigation took place within the glaciology section of the Alfred Wegener Institute Helmholtz Centre for Polar and Marine Research (AWI).

The field of glaciology is one part of earth sciences, covering all aspects referring to glaciers. The term glacier describes a stable body of ice at the surface of a planet-sized object. Examples for celestial bodies with observed water ice are Mercury (Chabot et al. 2014), Earth, Moon (Colaprete et al. 2010), Mars (Head et al. 2006), Europa and Enceladus (Prockter 2005). Research focuses at glaciers on earth, due to their easier accessibility and there high relevance for the earth's climate.

The domain of glaciers can be split into two categories. First the mountain glaciers and second the polar ice sheets. The obvious differences are their dimensions and location. In general ice sheets cover their surrounding terrain whereas mountain glaciers are found at locally restricted, high altitude peaks around the world. Other distinct features are their temperature range and flow velocities. The continental glaciers of Antarctica and Greenland are by definition the only currently remaining ice sheets on earth.
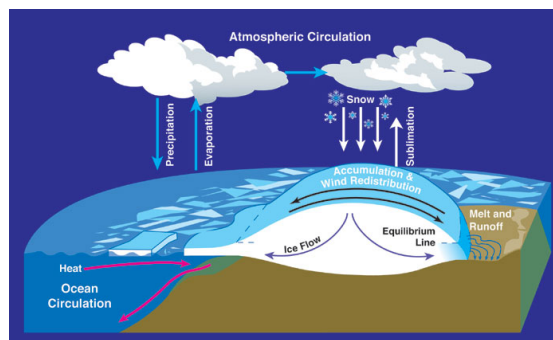

Figure 1.1.   Water cycle between atmosphere, glacier and ocean. (NASA 2005)

The role of an ice-sheet in the water cycle is shown in figure 1.1. This cycle starts with the accumulation of atmospheric precipitation, most common in form of snow, in areas with a year-round temperature below zero centigrade. There snow does not melt and get covered by another new layer of snow. The deeper the layer is advected, the higher the burden, generating a pressure which again leads to a compression. After initial breaking of the fresh snow crystals, the continuously rising pressure compresses the firn, which is by definition snow that survived an ablation period, till it is compacted by further processes, namely recrystallisation and creep, into glacier ice.

The close proximity to the melting point compared to other materials is one reason for the high plasticity of ice. This characteristic tries to balance the internal mass distribution by volume changes due to the incompressibility of ice. An initial ideal glacier shaped like a cube on a solid flat plain starts immediately to migrate towards its sides, if these are unconstrained. (Benn and Evans 2010)

Glaciers accumulating at locations with high altitudes get an additional forcing due to slopes. The ice on top of such slopes follows the gravity gradients towards the lower potential. Parameters effecting creep (internal deformations) are density, temperature and stresses created by the thickness and its gradient. Beside these always occurring internal deformations, sliding between glacier and bed and deformation of the bed itself are processes of glacial movement. The necessary condition for basal sliding is an unfrozen boundary between glacier and bedrock. In case of a temperate, sediment base, sheer stress can create deformations of the sediment in addition to sliding motion.(Benn and Evans 2010)

Reaching lower altitudes or lower latitudes, temperatures rises and some parts of the ice starts to melt. The melting process cools the ice but destabilises the ice structure. At the end of the glacier all ice is melted to water or breaks in the form of icebergs depending on the geography. Figure 1.1 sketches this mass flux in the water cycle.

Several investigations of glaciers around the world get performed to evaluate their fundamental characteristics. The wide variety of experiments reaches from the analysis of the micro-structure, and isotopic composition to global scale, high temporal resolution mapping. The mayor driver of these observations is the climate sciences. These are interested in glaciers due to their global influences on the energy and water balance as well as their function as a long-term atmospheric archive. Other fields focusing at fundamental laws of the flow-dynamic and processes within glaciers. One example of such a parameter is the internal velocity distribution. Figure 1.2 the changing trajectory of an initial imagined vertical line of individual marked particles (t_0 at the left hand side). As time moves on the particles moves, due to the flow of the surrounding ice. The difference between the bigger translations on top of a glacier can be explained by the higher sheer stress close to the bed. In case of a frozen bed the initial contact point would not move at all. Selecting the sliding motion typical for mountain glaciers and ice streams was done for a better visualisation. The relation between boreholes and this trajectory is further discussed in section 1.1: ice boreholes.
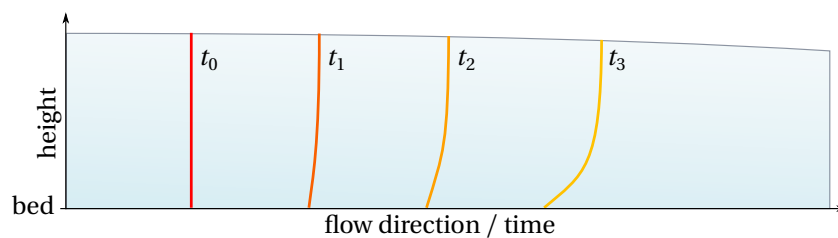

Figure 1.2. Diagram showing the evolution of a flow profile within a glacier of an initial vertical line or a borehole (Adapted from Benn and Evans 2010, p. 112). The profile shape depends on several parameters e.g. the boundary condition to the ground (frozen, slip, sliding), this profile relates to a sliding motion. Time moves forward to the right.

The deformation velocity, also referred as strain rate, can be generalised to a strain rate tensor. This tensor describes the change in deformation in each direction. Its two dimensional projection can be visualised by drawing circles on ice volumes in the horizontal plain and recording the changes in shape during their path throughout the glacier. A diverging flow for example compresses the initial round shape to an ellipsis with the semi-major axis perpendicular to the flow direction. Figure 1.3 shows the resulting pattern of this strain ellipses applied on a numerical model of the Midre Lovénbreen glacier in Svalbard by Ham-
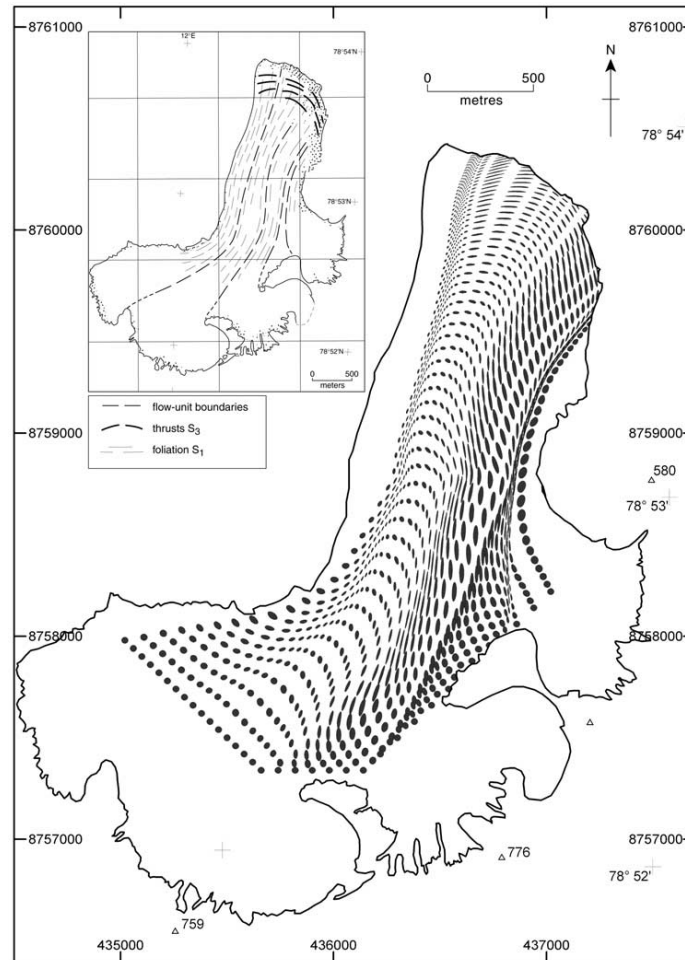
Figure 1.3. The strain-ellipse pattern illustrates the interglacial deformations from the glacier basin (lower part) towards the tongue (upper part). The shown data are based on a numerical model of the valley glacier Midre Lovénbreen, Svalbard (Hambrey et al. 2005). A borehole travelling with the flow get deformed like these strain ellipses.

brey et al. 2005. The initial circles are located at the accumulation area, lower part of the picture. The resulting complex pattern develops due to the different flow characteristics of this particular glacier, which is feed by three basins.

1.1. Ice boreholes

There are several methods to investigate the interior of a glacier, which can be distinguished into remote and *in situ* sensing. The major advantage of the remote sensing methods like ground penetrating radar or seismic surveying are their larger covering range and their lower cost. All of the remote sensing approaches are indirect methods, which mean that the investigated parameter like the height of the ice-sheet is detected by the measurement of another parameter. In case of radar the height is detected by the travel time of an electro-magnetic wave reflected by steep changes in the electrical conductivity of the penetrated material. This approach requires a good knowledge of the physical effects, the composition of the penetrated material and other environmental parameters. Therefore a calibration

based on independent measurements is required for reasonable results. This may be other remote sensing methods or much more significant, direct observations.

One of the best ways to observe a parameter is by a sample, measured in a laboratory with as many methods as possible. Sampling ice from the inside of a glacier requires a technique to access their location. The variety of tools spans from a hammer or hand-driven-drills to highly sophisticated machinery. This is especially true for the deep ice-cores drilled with electromechanical cable-suspended drills. An ice-core is a big continuous sample spanning from several meters to the entire glacier depth.

Electromechanical cable-suspended drills are typically composed of a rotating core barrel supporting a drill head with mounted cutters for cutting free an annulus around the core, supported within a non-rotating tube, a motor unit and an anti-torque section for transmission of torque into the bore wall. A winch at the surface moves the above described down-hole unit into the bore. (Johnsen et al. 2007)

Besides the just outlined electromechanical cable-suspended drills exists a wide variety of different drilling devices, such as auger (Koci 1984), hot-water (Bassler and Miller 1988), steam (Gillet 1975), compressed air, rotary drill rigs or melting probes. These techniques can be used for fast-access purposes like sampling sub-glacial water or the installation of sensors. One example for the combination of those technologies is the Ice-Mole from the department of aerospace technology from the University of Applied Sciences Aachen (Dachwald et al. 2014). It combines the melting-probe with a mechanical drill. The common feature of all mentioned technologies is the in most cases round borehole. These boreholes are either filled with melt-water, a different non-freezing fluid (Talalay and Grundestrup 2002) or the surrounding atmosphere, depending on purpose, kind of drill or depth.

Except from the refreezing case, boreholes offers a great opportunity for *in situ* measurements. Examples are the logging of a temperature profile (Philberth 1972) or seismic probes. In addition boreholes itself are useful probes. To understand this statement it may help to imagine the fundamental properties of a borehole.

In a first estimation a borehole is a vertical cylindrical geometry filled with a different material as the surrounding rigid material. Its circumference is much smaller than the height, which itself vary between a small fraction to the overall height of the glacier. The density difference between the hole and the surrounding ice can be rather high in case of dry hole or close to zero in case of balanced fluid filled holes. The selection of a drilling-fluid is based on their density which should be as close to the ambient density to balance the glaciostatic pressure of the hole and low viscosity to enable fast hoisting and reeving of the drill.

Ice is a viscopalstic material. Depending on the applied stress and the observed time scale ice deforms easily and does not appear to be rigid anymore. Therefore the borehole deforms over time like the particle path shown in figure 1.2. Measuring the orientation of the hole in small increments in combination with the depth allows the calculation of the path. Repetitions of this measurement over long time periods can be used for the estimation of the displacement distribution. Figure 1.4 visualises such a three dimensional path of an inclination measurement by Harper et al. 2001 of a valley glacier in Alaska. The measured initial path six days after drilling deviates from the ideal vertical line due to imperfections during the drilling process. The applied scaling may give a misleading impression of the achieved accuracy. The measurement at day 67 shows a descent flow profile.
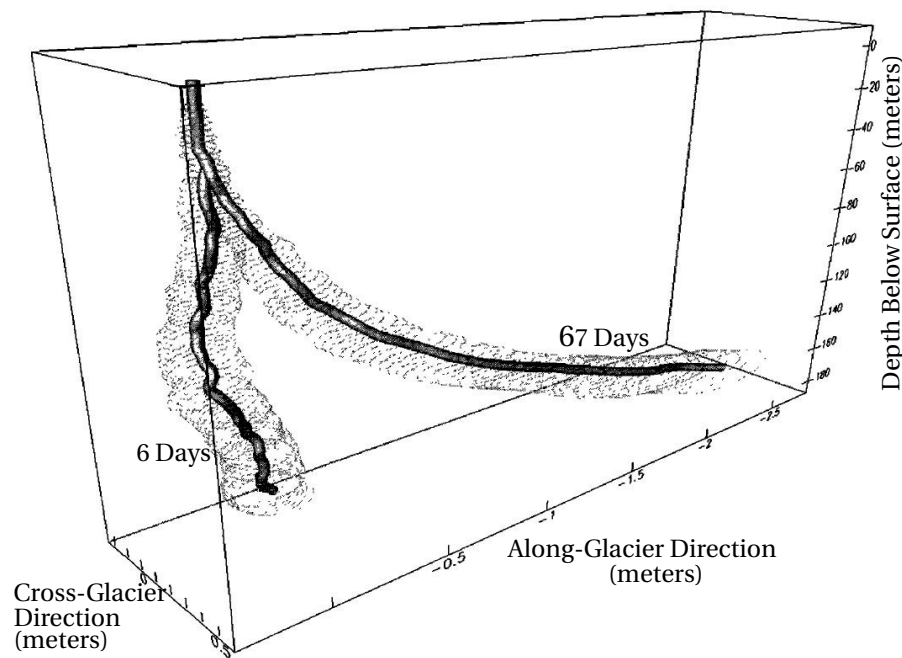
Figure 1.4. Example of an inclination measurement of a borehole 6 days and 67 days after drilling by Harper et al. 2001 at the Worthington Glacier, Alaska.

The second measurable parameter of a borehole is the mean diameter. Three lever calliper probes are the current state of the art diameter measuring probes. Their three levers are mounted in a equiangular radial pattern and are also constrained to a common movement resulting in a centring behaver. Assuming a circular shaped wall implies a relation between the hole-diameter and one lever radii. The EPICA borehole logger (Lefebvre et al. 2002) is one example for a probe measuring all parameters mentioned above. The biggest drawback of this type of probes is their required assumption of a circular borehole shape, which is reasonable for freshly mechanically drilled holes. Bores with other geometries could be created through rectangular melting-probes or variations in the heat flow of hot-water-drills. Another more interesting possibility is the deformation from the initial state by processes within the ice due to flow or refreezing.

A first attempt to measure this geometry in the field was done by Schwerzmann et al. 2006 with an eight-arm-calliper probe at Morteratsch- and Fiescherhorngletscher in the Swiss Alps. The mayor difference to the three-arm-calliper probes are the individual moveable arms. This mechanism does not centre itself but provides eight individual measured contact points. These logger coordinates complemented with the coinciding logger depth and orientation are the basis for computing a cloud of sampling points thus covering the hole wall. The wall shape can later be approximated by continuous functions like circles, ellipse, rectangles, etc.

The motivation for the current design of the 16 arm geometry and inclination probe are the double resolution of measured contact points in combination with a change of the basic sensor selection and the ability to log liquid filled holes with an overall depth of 3.5 km.

The next section 1.2 explains the concept of the measurement as well as some details of the mechanical setup as suggested in previous studies (Francke 2011, Francke 2012, Hüther 2012 and Hüther 2013).
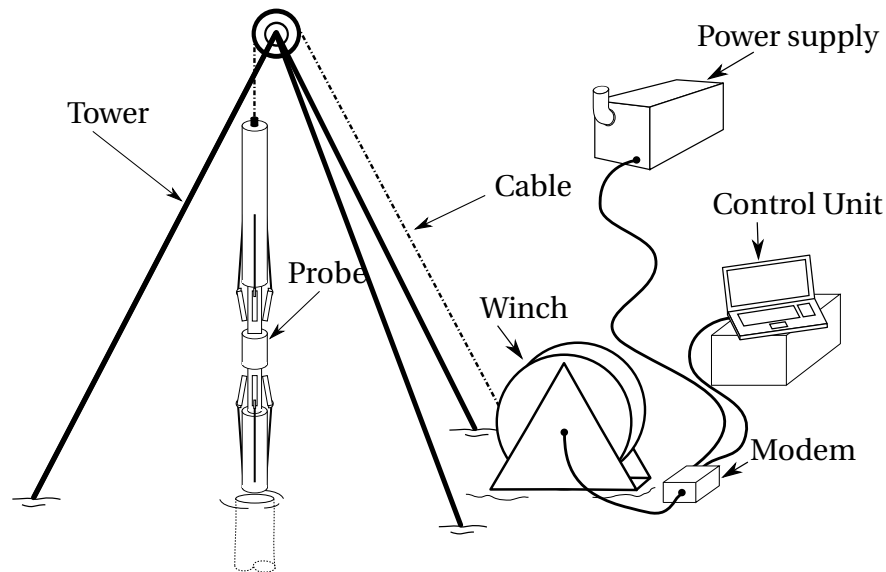
1.2. Concept

Figure 1.5. Principal components.

The principal components shown in figure 1.5 can be separated into a surface module and a probe. The surface module consists of a winch with cable, a tower, the power supply, modem and a control unit. Most components exist already from the drilling equipment. The winch moves the cable with the sonde through the hole and provides an electrical interface to the wire within the cable. The tower located above the borehole guides the cable and serves as a base for the winch. The communication link between the control unit and the sonde is established by two power-line modems. They provide a transparent Ethernet link as well as the power supply for the probe. Ethernet is a wide spread communication standard with a ubiquitous support from off-the-shelf computer hardware, therefore any available computer can serve as the control unit. The restricting factors are only the harsh general and climatic conditions during expeditions.

The probe sketched in figure 1.6 is a pipe with a diameter of 100 mm and a length of 1.5 m. Its upper part is a pressure resistant container, serving as an electronic compartment. The cable is mounted on the top end of this container. The lower part is a vented pipe to reduce the total length of the sealed assembly and with it the stress on the container wall. The assumed diameter range of the borehole varies from 110 to 250 mm leading to an initial alignment between probe and hole. Figure 1.7 shows an inclined hole with the first
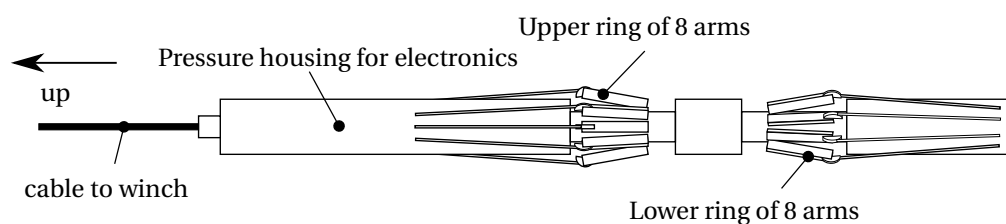

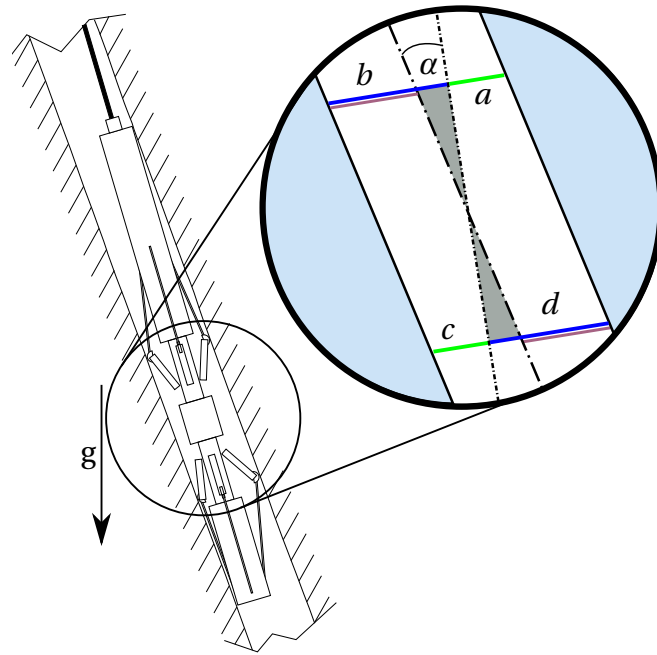**Figure 1.6.** Schematics of the probe.

Figure 1.7. Probe in inclined borehole.

generation of the probe. A trigonometric treatment estimates the maximal misalignment in bores of up to 250 mm to be less than approximately 6°.

Prior inclination loggers, e.g. like *the EPICA borehole logger* (Lefebvre et al. 2002) eliminate this error by incorporation of a centring mechanism on both ends of the logger. The new type of geometry logger should be able to measure the actual deviation. Nevertheless, provides the option for further development of some kind of centering mechanism to increase the performance and to prevent the probe from oscillations within the bore. The borehole inclination reduces to a measurement of the angle between the vertical and the probe axis and its orientation.

The borehole geometry is measured by individual levers/arms pressed against the wall. The determination of each lever distance consists of an angle measurement, followed by a trigonometric calculation. This calculation requires the knowledge of the lever length and the position of their joints. The probe has 16 levers in total, spaced equidistant over the circumference and arranged in two planes. The resulting resolution, of the cloud of 16 contact points, depend on the diameter and the *real* shape of the borehole wall. Therefore it may not be able to determine any arbitrary highly irregular shape. Nevertheless, this is a big step forward compared to the eight-arm calliper–inclinometer (Schwerzmann et al. 2006) used in dry boreholes and a huge step from the three-node circumscribed circle fitted diameters, combined with the course from integrated inclinometer readings and the measured depth, inclinometers used in the deep boreholes in Antarctica or Greenland (Grundestrup et al. 1994 and Lefebvre et al. 2002).

Splitting the arms in to two rings was necessary to provide enough spacing between them, together with the additional blockage protecting system. This arrangement is also able to measure the deviation (α) between the probe alignment and the borehole axis. Figure 1.7 illustrates the geometrical calculation of α from the middle point of the eight arms on each ring together with their vertical separation.

1.2.1. MEMS – Microelectromechanical systems

One distinguishing characteristic of this geometry logger compared to its precursors is the introduction of micro electromechanical systems or short MEMS as the most used sensor technology. Therefore it might be useful to understand some of their basic properties. First of all the abbreviation MEMS describes a whole field of technology, covering every system using electromechanical effects on the micro scale. Typical package sizes of those structures are comparable to small electronic circuits. Their small size makes the mechanical deployment easier. The big advantages of scaling closer to the micro level are increasing small size effects like the electrical capacity between surfaces. At the same time, materials with a high quality become available as well as the precision of the mass production processes increases. A typical technology to machine such structures is the lithography using electromagnetic waves at specific wavelength to process the material. This technology evolved with the need of the computer chip industry for their smaller and smaller circuits, which now reaches to the nanometer level.
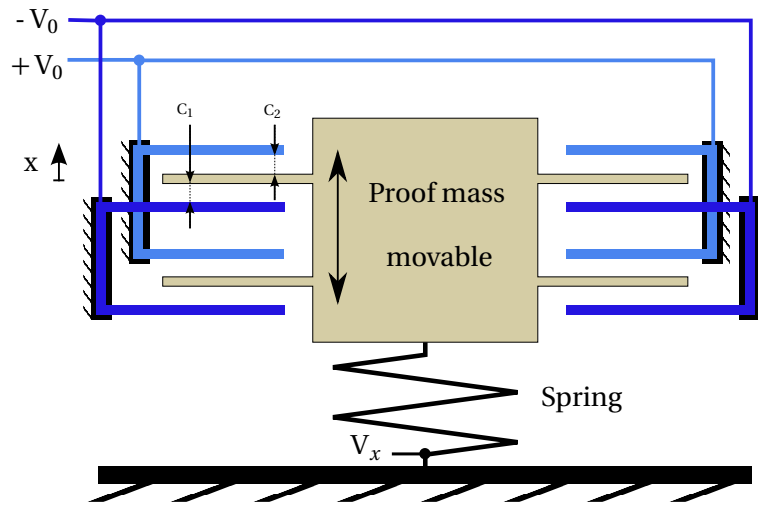
Figure 1.8.   Schematic of a MEMS Accelerometer. (Adapted from John 2011)

Apart from some original small size effects, most principles from *normal* sized applications are adapted. A good example is the accelerometer. A prove mass mounted on a spring senses any acceleration by a displacement. Measuring the distance of the movement allows to infer to the value of the acting acceleration by using Newton's laws of motion:

$$\vec{F}_a = m\vec{a} \tag{1.1}$$

combined with Hooke's law:

$$\vec{F}_s = -k\vec{x} \tag{1.2}$$

The used variables are the acting force ($\vec{F}_s$ and $\vec{F}_a$), the mass (m), the acceleration ($\vec{a}$), the proportional spring constant (k) (valid until the elastic limit) and the deformation length ($\vec{x}$). Setting $\vec{F}_s = \vec{F}_a$ leads to equation:

$$\vec{a} = \frac{-k\vec{x}}{m} \tag{1.3}$$

This or a similar approach is widely used in common accelerometers. In MEMS this kind of sensor profits from the high reproducibility of mass production and is also able to measure small changes in distance. One example for such a measurement principle is the capacitive distance sensing, which is sketched in figure 1.8. The proof mass consists of a solid body with small ribs on the sides. It is framed by fixed counter-ribs. A rib counter-rib pair works like a parallel-plate capacitor. The related equation is:

$$C = \varepsilon_r \varepsilon_0 \frac{A}{d} \tag{1.4}$$

where C refers to the capacitance, ε_r to the relative static permittivity (material between plates, e.g. vacuum $\varepsilon_r = 1$), the electric constant ($\varepsilon_0 \approx 8.854 \times 10^{-12}\,\mathrm{Fm}^{-1}$), A as the overlapping area and the separating distance (d). Generating a reasonable high capacitance for the measurement system requires a large area as well as a small distance between the parallel plates. Measuring a movement requires a certain lower limit of the separating distance therefore the area has to be increased, which can be done by adding more and more ribs. Figure 1.9 should give an impression of the structural dimensions.

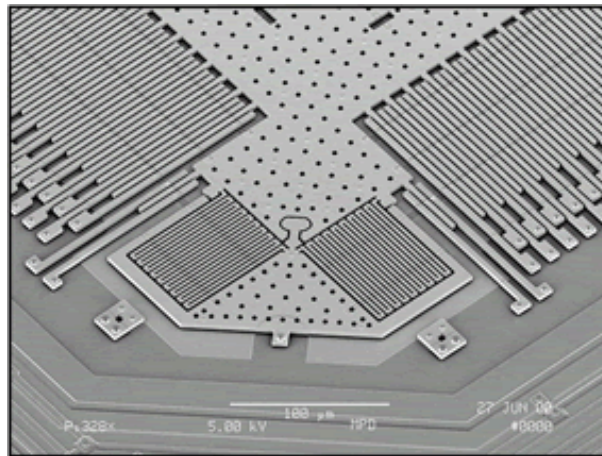Appendix A contains a further derivation of this distance measurement.

Figure 1.9. Partial photography of a MEMS Accelerometer. Illustrates the structural dimensions, the white scale in the lower part shows $100\,\mu$m. (Princeton.edu 2007)

The use of common manufacturing methods from integrated the circuit industry suggests a combination of the sensor with its custom evaluation circuit. This driver circuits provide a set of digital or analogue interfaces and some configuration options. This is a distinguished feature compared to analogue sensors requiring a separate converter.

Except from these advantages exist some drawbacks. The first are their manufacturing methods. All of them require high accuracy and precision as well as cleanroom conditions, which makes an installation expensive. This can only be economical in a mass production for example for the entertainment industry or other high quantity markets. The above mentioned accelerometer used mostly in mobile phones or hard-drives, is a good example. Special needs of the scientific community is hardly recognised.

An additional problem got introduced due to their small size resulting in relatively high noise levels. The accelerometer has three main noise producing parameters, the signal conditioning circuit, the vibrations produced by the springs and from the output measuring system (John 2011).

The third and last mentioned disadvantage refers to the all in one solution resulting in some sort of compromise. Their is also no possibility to change one sub component, e.g. the A/D converter. All in all MEMS can be a valuable option in case of an available solution with a required performance already exists and time for the firmware development can be afforded. This probe serve, beside of its measurement capabilities, as a test platform for the integration of MEMS-based sensors.

1.2.2. Parameters

This section gives an overview about the each measured parameter and its acquisition method. Starting with the depth, temperature, inclination, orientation and finally the shape.

Depth

Sensing the depth of the probe is performed by two independent means. The first is a measurement of the cable length by the use of a rotary encoder at the tower. This method provides a measure of the length. Assuming a stiff cable and a perfect vertical hole, the path is equal to the depth. In the real world this path varies from the true value. Reasons are thermal dilatation, elongations of the cable created by the increasing load caused by the cable weight and the deviations of the borehole axis from the vertical alignment.

The second method uses two pressure sensors mounted in the probe. The gauges are selected for the operation in fluids. There the environmental pressure rises steeper then in the atmosphere with an increase in depth. The resulting pressure signal can be translated in a depth by the Pascal's law (eq. 1.5). The required input parameters are the fluid density (ρ), the level of the fluid and the atmospheric pressure (ρ_0) at that level. Disadvantages are the required wide pressure range of the sensor and the unknown density of the medium.

$$p(h) = \rho g h + \rho_0 \qquad (1.5)$$

To enhance the possible accuracy, the second identical gauge mounted approximately one metre apart. This additional signal is used to measure the pressure difference and with it a estimate of the local density. Equation 1.6 can be derived by substituting 1.5 into $\Delta p = p_2 - p_1$ assuming a constant density between the sensors.

$$\rho = g \frac{\Delta h}{\Delta p} \qquad (1.6)$$

As the density is proportional to the derivative of pressure with depth, the integration of $\mathrm{dp}/_{\rho g}$ provides an independent depth scale, that depends on the distance between the sensors, the precision of the measured pressure difference, the knowledge of local acceleration of gravity and the precision of the pressure measure.

Temperature

The design of the borehole logger includes an interface for a temperature logging module. This module itself is not provided in this work and can be seen as a further improvement. Nevertheless an on-board temperature sensor is implemented inside the probe. Its signal is part of the housekeeping data and does not fulfill scientific demands. Therefore it only gives a ruff impression about the current conditions and can be used for calibrations.

Inclinometer

The direction vector of the probe is measured by its inclination. This is the angle between the vertical axis and the probe axis. The vertical axis is represented by the gravitational field pointing to the earth center, which can be observed by the acceleration acting on a test mass. The measured acceleration is always a combined signal, this means that a sensor not distinguishes between the source of the acceleration. To ensure that the measured acceleration is approximately the gravitational signal requires an elimination of all other disturbing sources. The biggest disturbance is related to the movement of the probe.

Prior inclinometers consist of a test mass mounted at a lever on a system of gimbals. The inclination was then measured by potentiometers and high resolution analogue to digital converters. Such devices require a big volume within the probe and have mechanical issues like the gimbal lock.

The design contain in total nine MEMS accelerometer of the type BMA280 from Bosch Sensortec^{TM} serving as inclinometers. The BMA280 was selected due to their analogue to digital converter resolution of 14 bit over a range of $\pm 2\,g$. The number of nine splits into eight external mounted sensors, contributed by the selected geometry estimation method (see 1.2.2) and one base sensor. This base sensor is located inside the electronic pressure housing. The higher noise level of the MEMS compared with traditional sensors can be reduced by using the higher number of probes and a statistical analysis.

Orientation

The orientation of the probe referring to global coordinate system is required to enable a transformation of the sensor data. Compasses are the most used instrument on earth to solve this task. They sense the horizontal direction of the magnetic field of the earth. Due to the proximity to the magnetic poles, the magnetic field points mostly either towards or outwards the ground. Using a three-dimensional magnetic field sensor in addition to the inclination data will increase the accuracy of the orientation. The local offset of the earth-magnetic-field has to be done manually by measuring its direction during the calibration or by pre-recorded data.

The second MEMS based sensor is the inertial measurement unit (IMU) BMX055, containing three different three-axial sensors: an accelerometer, a magnetometer and a gyroscope. This sensor unit is used as a tilt compensated compass to measure the probe orientation. Its accelerometer has a lower resolution as the one in the BMA280, therefore another BMA280 accelerometer was added next to the BMX055. The reason for selecting the combined sensor was the additional gyroscope, measuring the rotation rate. Integrating the rotation rate over time resulting in the total changed orientation angle. This method is only useful in short term applications, due to small errors in the measurement leading to large discrepancies in the long term integrated signal. Nevertheless is this signal a pretty good parameter for the quality of the gathered data in general. In case the gyroscope senses some value other than zero implies an acting acceleration other than the pure gravity. Therefore this can be used as flag for a *damaged* dataset and maybe useful for noise cancellation of the magnetometer.

Angle of levers - distance to the borehole-wall

The measurement of the distance between probe-axes and borehole-wall on each contact-lever is performed by a set of two three-dimensional accelerometers. The first sensor called reference sensor is located within the probe and the second named arm sensor is mounted in the lever. Both sensors are oriented in the same plane as shown in figure 1.10. They measure the same acceleration vector in different coordinate systems. The differences in the signal depend only on the rotation between the two sensors, which can also be expressed as an angle. This new sensor arrangement compared to more traditional potentiometers has the advantage of using a probe independent parameter. Translational disturbances do not change the resulting angle, due to the synchronous effect on both sensors. This cancellation will not work in case of angular accelerations. Therefore the further centering mechanism preventing oscillations and the additional gyroscope for detecting the current rotation rate are reasonable additions.
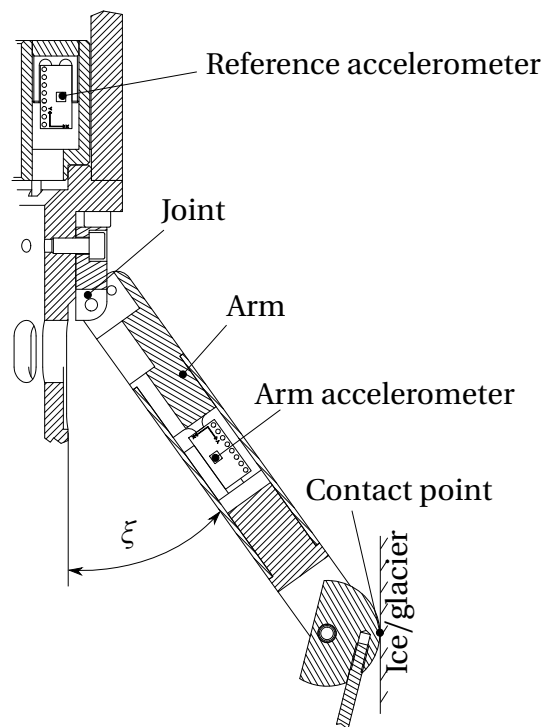
Figure 1.10. Assembly of the distance measuring arm.

Each arm accelerometer has a reference sensor in its plane to reduce the complexity of coordinate transformations during the measurement. Minimising the amount of sensors is also possible by sharing one reference sensor with two opposing arm sensors. The total amount of used accelerometers is 25, which composes from 16 arm, eight reference sensors and one base sensor in the electronic pressure housing.

The measured distances can be transformed into a point cloud around the path. This requires the joint alignment, the orientation within the borehole as well as a depth and inclination profile. Figure 1.11 shows one possible attempt for a data analysis. There a regression ellipse of all contact points was calculated as suggested in Schwerzmann et al. 2006. This setup enables the implication of differential flow within the ice.

Figure 1.11. The schematic shows all five parameters describing a regression ellipse, seen from the probes coordinate frame. The parame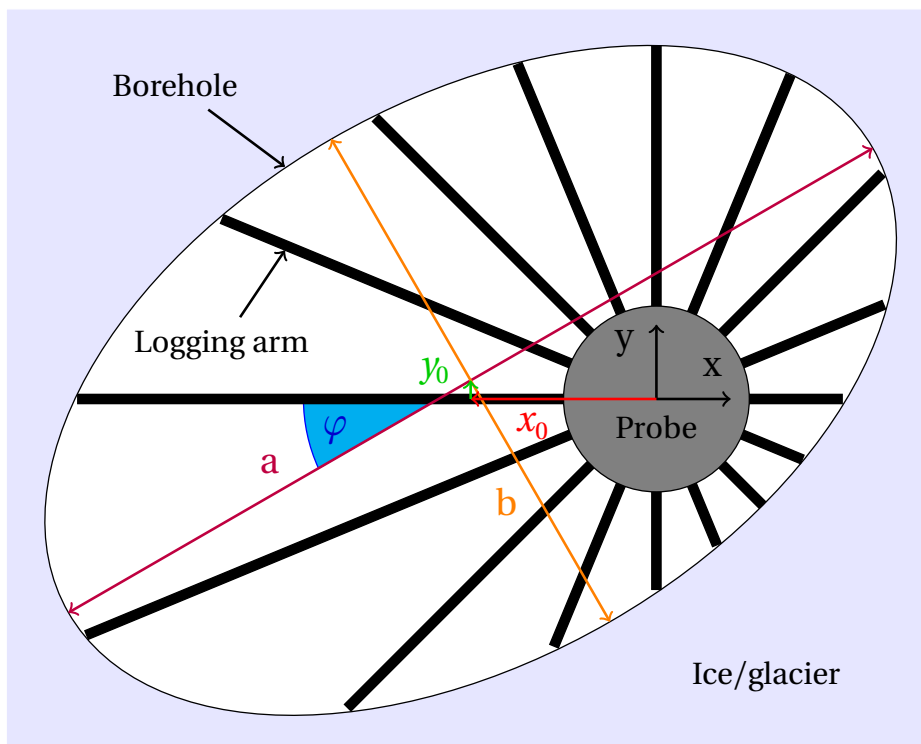ters are semi-major axis (a), semi-minor axis (b), tilt angle of the ellipse (φ) defined counter-clockwise from x-axis and the offset of the ellipse center (x_0 and y_0) (Adapted from Schwerzmann et al. 2006)

2. Hardware

The main function of the electronics is to interface to each sensor described in chapter 1.2 as well as providing a communication link to the surface unit and a data storage. The requirements for the electronic design are:

- Data acquisition cycle of half a second.

- Synchronous and ordered data storage on-board and on the surface station.

- Interface to sensors:

Sensor type	External	Pressure housing	Surface station
Accelerometer	24	1	
Magnetometer		1	
Gyroscope		1	
Outside pressure sensor	1	1	
Barometer for leak detection	1	1	
Array of thermometers	1		
Borehole bottom contact switch	1		
Encoder			1

Table 2.1. List of used sensors.

Transmitting all data from the remote sensors to the electronic pressure housing requires a stable transmission protocol. The selected BMA280 accelerometers support only SPI and I^2C interfaces, which are suitable for the communication between controllers in close proximity. Therefore a different kind of interface has to be added to the sensor. Another driver for the selection process of this interface is the amount of individual wires, due to the limited poles of the selected connector. Some available standard interfaces are summarised in the following table:

BUS	RS-232	RS-422	RS-485	CAN-BUS
Mode of Operation	single-ended	differential	differential	differential
Duplex transmission	full	full	half/full	half
Wires	3/5	4	2/4	2
Max. devices	1	10	32	-
Network topology	point-to-point	multi-point (addresses)	multi-point (addresses)	multi-master (messages a. priority)

Table 2.2. Comparison between standardised interface buses. Source: *ANSI/TIA/EIA-422-B-1994* n.d., *ANSI/TIA/EIA-485-A-98* n.d. and *CAN Specification* 1991.

All mentioned standards are serial interfaces, due to their reduced number of wires compared to parallel interfaces. The most common serial interface around personal computers is the RS-232 standard. This is useful for point-to-point connections in a moderate environment. The CAN-BUS located at the other side of the spectra, build for the harsh environment in cars combined with the need of high reliability. This requirements lead to a sophisticated protocol designed for data safety and interchangeability of nodes. This comparably large overhead in the protocol leads to an unnecessary complexity of the design. Between this extremes are the related standards RS-422 and RS-485, which are widespread in industrial applications. Both are designed to extend over long distances in noisy environments. This is achieved by using differential signal wires. In contrast to the fully defined standard RS-422, the RS-485 provides the possibility to choose between a half and a full duplex mode. Full duplex describes the ability of a simultaneous receiving and transmitting operation on individual wires, compared to the request/response behaviour of the half duplex system. Identifying the single acquiring processor, at the end of the bus interface, as the bottleneck of the system, result in a highly managed data acquisition loop. Requesting one slave at a time removes the advantage of speed from a full duplex operation compared to the reduced number of wires of the half duplex version.
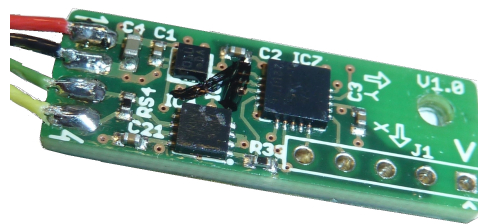

Figure 2.1. BMA280 accelerometer board with controller and RS-485 Bus driver.

The need of a custom protocol requires also a controller, translating between the sensor interfaces and the bus protocol. The burden of having an additional controller in the system, which costs initial development time, results in an increased modularity of the overall system. A change in sensors, result in a patch of the controller and data acquisition module firmware. This intermediary controller makes additional data adjustments possible. The selection process of the adjustment method is covered in detail in chapter 3.1.1. The idea of a highly modular system became introduced to the remaining sensors within and outside of the electronic pressure housing, resulting in the electronic design sketched in figure 2.2.

The electronic compartment (big blue box) contains the *heart* of the system labelled with main board. It is a fast controller with on-chip Ethernet, flash memory and USB support, running the data acquisition loop. This loop is responsible for the timing and the collection of all sensor data. The Ethernet stack is necessary to communicate with the ground station, providing additional data of the encoder and control commands. The available fast data link to the ground unit enables the additional mirror of all collected data at the ground station. To achieve a necessary data security a copy gets stored on a local flash memory card as well. Mirroring the data on the ground station makes *live* visualisation during the operation possible. This can be helpful during the testing phase and provides an easy understandable functionality check in the field.
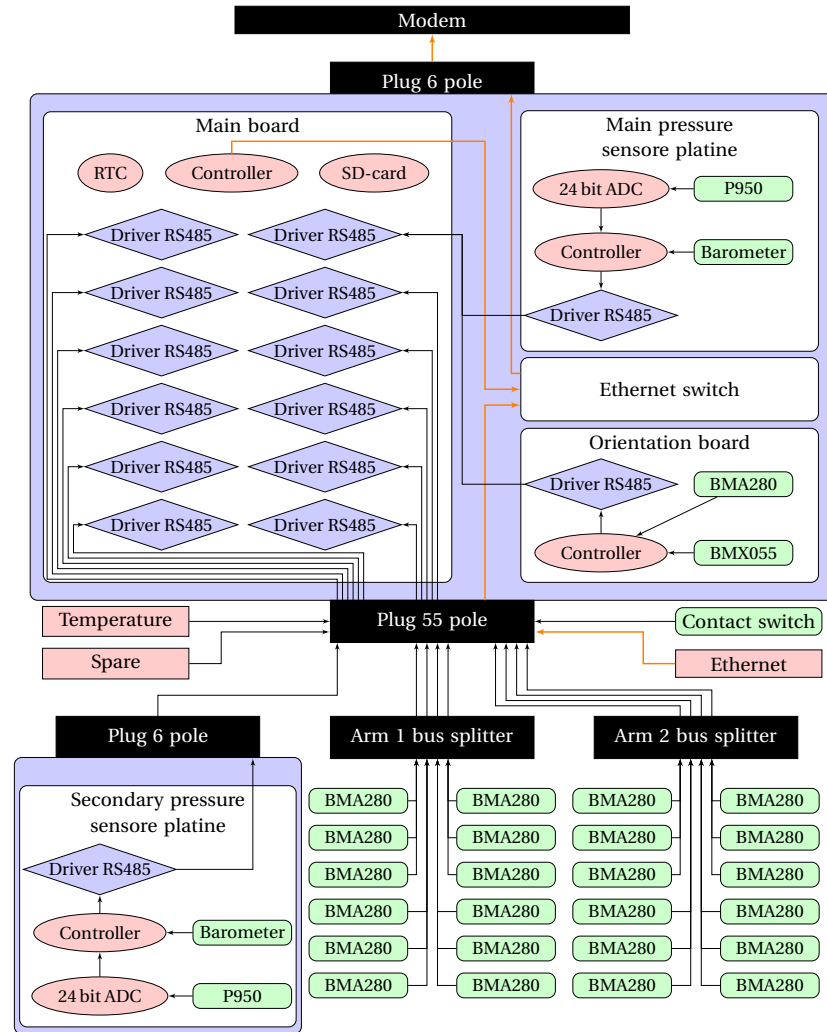
Figure 2.2. Scheme of the logger electronic interface structure.

In case of a lost transmission or other data corruption at the surface unit, all data can be accessed either via reading the SD-card or by switching polarity of the power supply, changing the operation mode of the probe from Ethernet logging to an external USB mass storage.

The real time clock labelled with RTC guarantees a correct data synchronisation between the surface unit and the probe. The remaining major area of the main controller board is covered by a cluster of interchangeable RS-485 network driver boards. These driver boards enable the main controller to communicate with all connected sensors.

All internal sensors are spread over two boards communicating via a RS-485 bus with the main board. The so called *orientation board* contains the base accelerometer (BMA280) as well as the gyroscope and magnetometer (BMX055). This board is mounted at the lower lid of the electronic pressure housing above the 55 pole plug. The lower lid has a unique position in the probe construction. On the lower side hangs the lever mechanics for the geometry measurement and on the upper side mounts the support structure for the electronic boards. Therefore it is a well-defined place in the construction serving as the origin of the main, body-fixed coordinate system. In addition to its defined location and orientation, it is the

most rigid point of the support structure, reducing vibrations of the sensors.

The upper lid holds the upper pressure sensor (P950), a barometer for the leakage test and a 6 pole plug for the power supply and the Ethernet/USB connection. Due to the analogue nature of the pressure sensor, an analogue to digital converter (ADC) with a resolution of 24 bit is required to translate the sensor signal for its controller. Reusing this pressure sensing part for the lower pressure sensor in the second container (small blue box) could be done by separating the power switching, fuse and data handling part from it. Figure 2.3 shows the comparison between both versions.
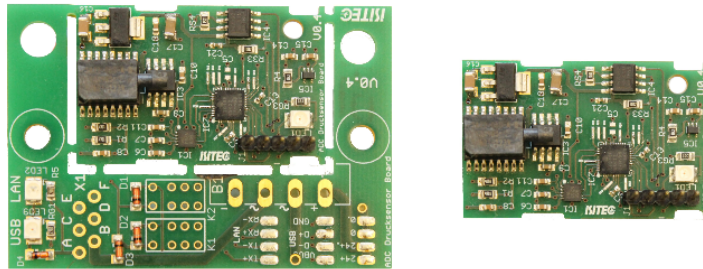

Figure 2.3. Comparison between the upper pressure sensor board with power part (left) and lower pressure sensor board (right).

The accelerometers of the geometry measurement, located either within the arms or in the reference body, are connected to different serial communication buses. The first division is into the two measurement rings holding their own distribution board. One ring consists of four reference sensors and eight arms is further subdivided into four individual RS-485 buses. Each accelerometer bus handles one reference sensor and the two related arm accelerometers. The resulting data loss of a single bus failure reduces than to only two opposing contact point pair. Another reason is the data handling by sensor addresses. The interchangeability of the sensor ports (RS-485 interface shown in figure 2.4) requires a fixed sequence in the sensor address space to differentiate between the sensor positions (for more details refer to chapter 3.1).

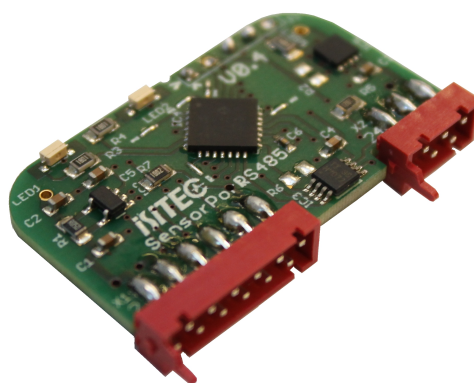
Figure 2.4. RS-485 Driver board.

The remaining interfaces, like the temperature board or the Ethernet bypass are reserved for further extensions.

The electronic layout of the boards was made by an external supplier in a close feedback loop.

3. Software

The software for the logger is divided into two major parts, the data acquisition from the sensors to the main controller and the transfer to the surface module. The second part, located in the surface unit, transforms this raw data into a useful data format, calculate, derived parameters and displays the results. All components are shown in figure 3.1.

The upper section including the probe/TCP receiver module and the encoder with its corresponding server are part of the data acquisition part. The associated hardware increases in complexity from the small eight-bit interface controller, over the RS-485 bus network and main data handling controller to the PC used as the surface unit.

The modules 'Control' and 'Visualisation' represented in the green box of figure 3.1 in addition to the 'Translate Logger Data' module, are implemented in the second software part. These modules are all optional mere software blocks, represented as applications on the surface unit.
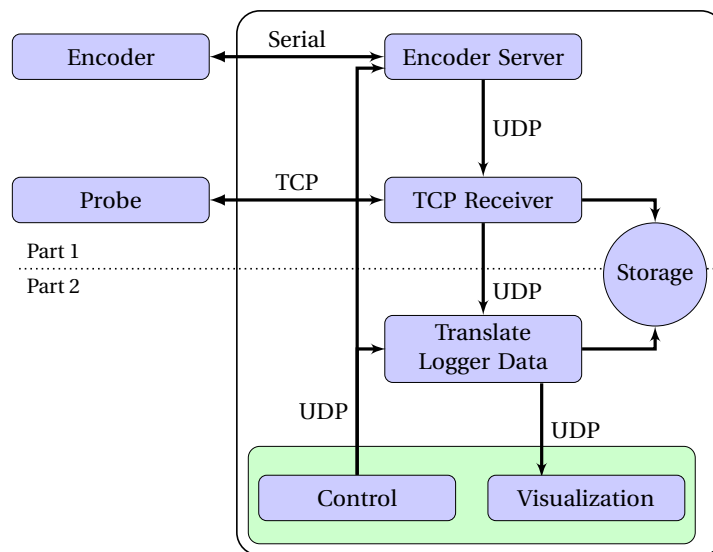
Figure 3.1. Data flow in the surface unit.

Communication between the modules is handled by the Ethernet network protocols TCP and UDP. TCP or transmission control protocol has a connecting transmission model providing a guaranteed data delivery in contrast to the connectionless user datagram protocol. Therefore the high data reliability requirement of the communication between probe and surface unit uses TCP. In contrast to the UDP based visualisation chain, were a dropped dataset results in an update gap whereas a re-requested package may change the update order. In all cases the raw data of the logger are stored in the surface unit and in the probe, being available as possible original measurement dataset for the post-processing.

Different additional software exists to perform tasks like the programming and configuration of the sensors.

3.1. Data acquisition

The main controller of the probe needs to support two different modes of operation. Mode 1, running the data acquisition loop, and mode 2, distribute all stored data as a USB mass storage device. Figure 3.2 A describes the overall routine of the firmware including the subroutine '*DAQ loop*'. This subroutine, expressed in more detail in part B of figure 3.2, gives a clear picture of the program flow. The accumulated data of each cycle includes all sensors values, a time stamp for synchronisation as well as the received data from the surface station. In case of a permanent failed connection to the surface unit, the acquisition of the sensor data continues until the loss of power.
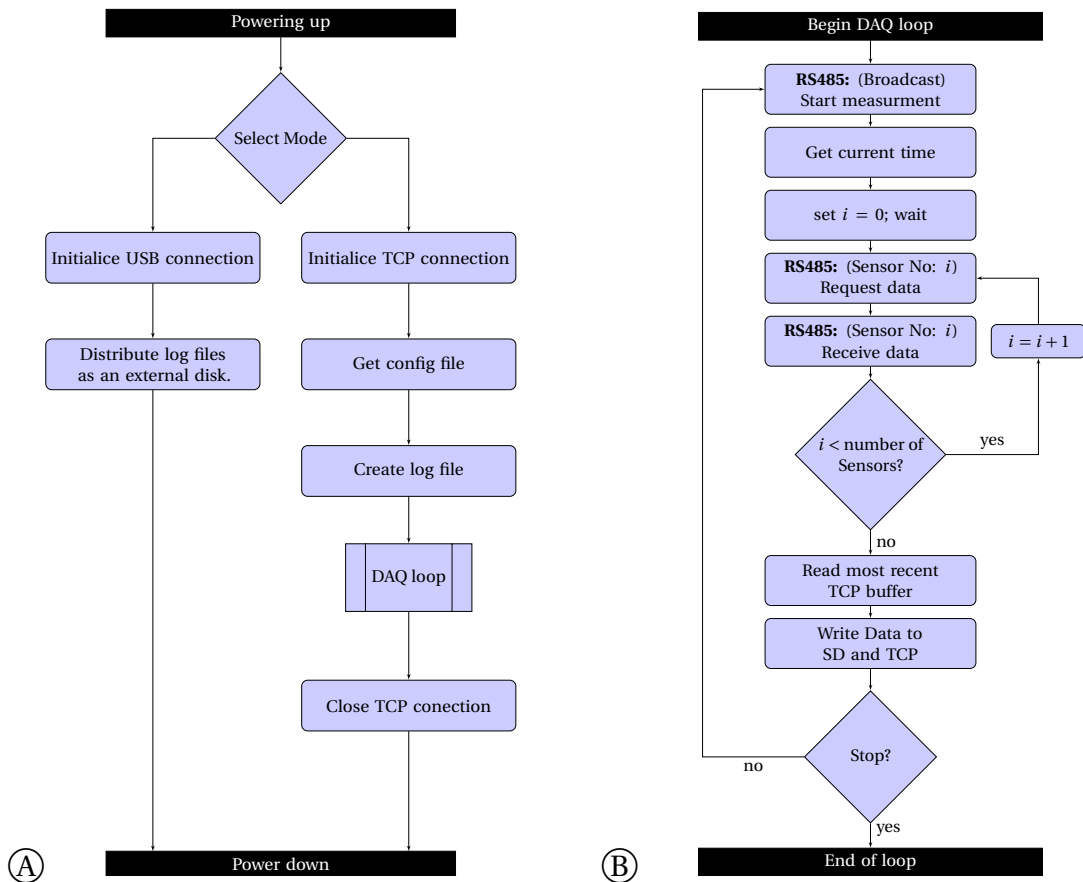
Figure 3.2. Program sequence on the main controller of the probe.

The actual measurement loop is required to perform within the cycle time of 500 ms. Weighing factors of the cycle time selection are the achievable resolution in depth, which also depend on the probe velocity and the sensing and transfer timing of all sensors. The relatively long interval was chosen, due to a high number of unknowns in the timing behaviour. This 500 ms interval leads to a resolution of 5 cm with a logging velocity of 10 cm/s. This velocity corresponds with a one-way log time of approximately one work day (< 10 h) per 3.5 km deep hole.

The designed data handling protocol on the RS-485 bus supports a common synchronous message starting the measurement. This broadcast signal accomplishes a consistent parallel data acquisition. After a delay for the measurement each sensor gets requested individually, due to the limited sequential processes in the bus and controller.

3.1.1. Statistical data acquisition method

Referring to the selection process of the sensor bus interface in chapter 2, each sensor has an individual driving controller. The dedicated controller sitting next to the sensor is able to interact much faster than the main controller and the acceleration sensors itself sampling full three-dimensional acceleration vectors at a maximal rate of 2 kHz (*BMA280: Data sheet* 2013). Taking advantage of these facts allows an implementation of a pre-filtering of the sensor data. One of the simplest methods would be an averaging by calculating the arithmetic mean (equation: 3.1). This method removes small variations introduced e.g. by noise. Averaging over a long time period will also reduce the resolution in time. Therefore the number of measurements (N) has to be limited.

$$\bar{x} = \frac{1}{N} \sum_{i=1}^{N} x_i \tag{3.1}$$

x_i : value of a single measurement
$\bar{x}$: arithmetic mean
N : number of measurements

An additional parameter for the scatter range would increases the expressiveness of such a mean value. One example for this kind of parameter is the absolute range of the sensor data. Recording the minimal or maximal values does not address the more important question about the statistical distribution of the recorded data. The standard deviation expressing a probability range is therefore a better choice, when the data is random. For noisy sensors this is a valid assumption, due to their dependency on multiple independent variables. Literature defines the standard deviation in different ways, this document adopts the nomenclature of the statistics book by Barlow 1989, there the *standard error of the mean* ($\sigma_{\bar{x}}$) is defined as:

$$\sigma_{\bar{x}} = \sqrt{\frac{1}{N(N-1)} \sum_{i=1}^{N} (x_i - \bar{x})^2} \tag{3.2}$$

Another equivalent option of expressing this formula is equation 3.3 by applying the Steiner translation theorem.

$$\sigma_{\bar{x}} = \sqrt{\frac{1}{N(N-1)} \left[\sum_{i=1}^{N} x_i^2 - \frac{1}{N} \left(\sum_{i=1}^{N} x_i \right)^2 \right]} \tag{3.3}$$

There are different approaches implementing this statistical sampling method on the micro-controller. The resulting parameters $\bar{x}$ and $\sigma_{\bar{x}}$ has to be logged in each sampling cycle for every sensor dimension. From the statistical point of view an infinite number of samples at a single location would result in the best achievable solution. Moving up- or downwards in the hole contradicts such a long measurement period and a stop and go procedure takes much too long and may introduce additional disturbing accelerations for the inclination measurement. In all cases an averaging and statistical analysis requiring multiple samples of each parameter results in a sample span rather than a sample point.

Sampling a full buffer size of 32 samples of the accelerometers at their maximal sample rate of 2 kHz corresponds to an overall measurement time of 16 ms, which is also a sample length of 0.16 mm by assuming a logging velocity of 10 cm/s. Reading multiple buffer sizes leading to a higher accuracy of the standard error of the mean requires additional time for the measurement and increases the sample length. The data transfer of all sensors can at earliest start after passing the time period required by the measurement plus data transfer to the controller and running the statistical algorithm. In addition to this time the overall data transfer over the bus network needs also a relatively long time and has to be performed within the defined 500 ms. Keeping this in mind lead to the decision to use one full buffer size of 32 samples in the first iteration of the software. Evaluating the necessary timing of all steps of this version could later be used to adapt either the cycle timing or the amount samples within this cycle.

Minimising the runtime of the algorithm on the sensor controller is the most important step before applying this statistical method. Reviewing equations 3.2 and 3.3 shows a first unnecessary and numerical costly calculation of the square root during each cycle. This operation could be done at the surface unit or in the post-processing if the squared number got logged instead.
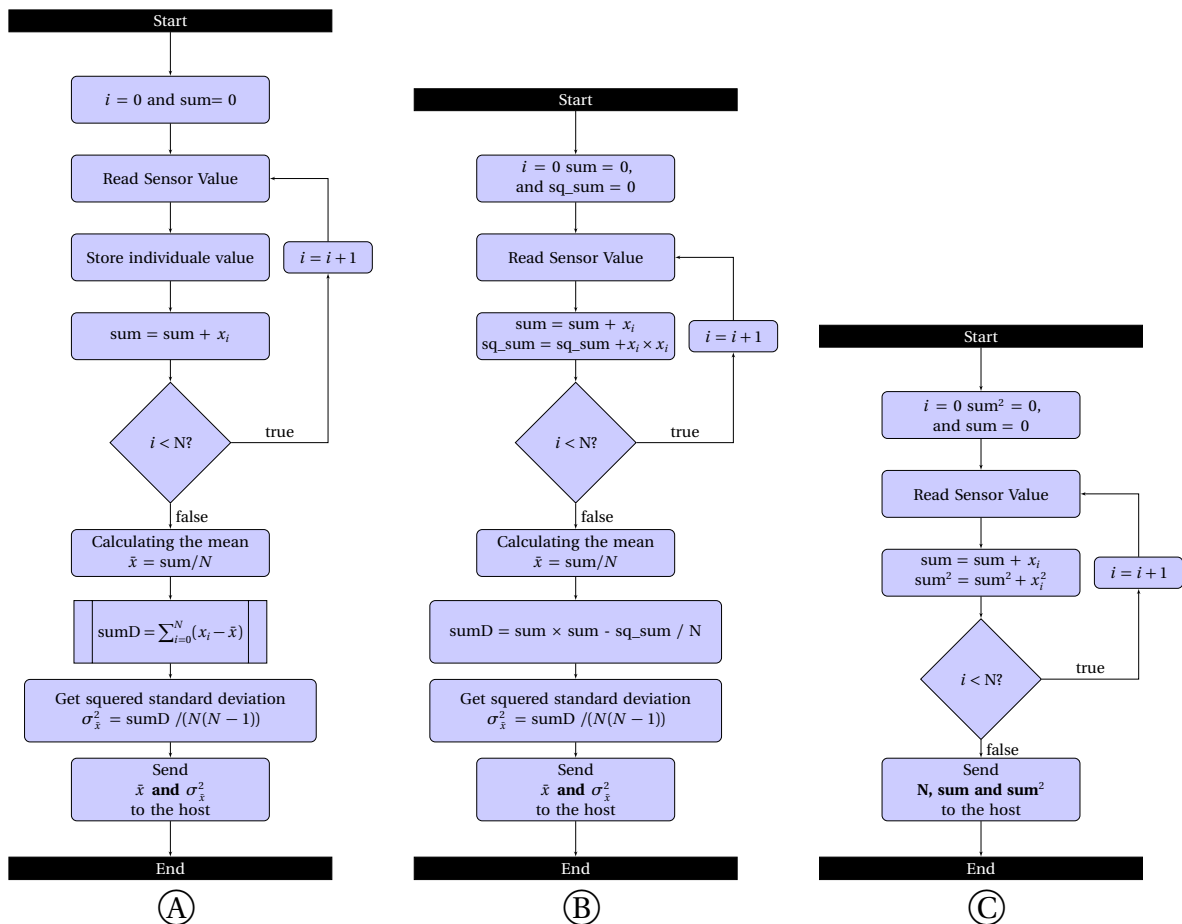

Figure 3.3. Comparison between three approaches of a statistical sensor analysis. A shows the analysis with two parameters using equation: 3.2, B the related method using equation: 3.3 and the three parameter transfer method in C.

A first attempt of calculating both required parameters $\bar{x}$ and $\sigma^2_{\bar{x}}$ directly on the sensor controller using either equation: 3.1 or 3.2. Figures 3.3 shows their algorithm as a flow diagram and appendix B contains the associated code examples.

Algorithm A using equation 3.2 requires a high performance and a high storage capacity to hold every value during the whole calculation. The storage capacity of a small eight-bit controller limits the number of samples especially in the case of three dimensional sensors. The storage problem could be solved by using algorithm B of figure 3.3, using equation 3.3. This algorithm has a different disadvantage by requiring rather large data-types for the variables storing the result of $\sum x_i$ and $\sum x_i^2$ resulting from the high resolution of the sensors and the selected sample number. This characteristic could result in buffer overflows, if the amount of samples does not correspond to the resolution and sample number.

The second bottleneck of a small eight-bit micro-controller is its low performance in the handling of higher order operations on floating point values. The complexity of algorithm B can be reduced by changing the assumed transfer protocol and send three instead of two values per dimension over the bus. This will increases the transfer time but reduces its algorithm further into C, computing just $\sum x_i$ and $\sum x_i^2$. The third and last statistically important property necessary for the computation of $\bar{x}$ and $\sigma^2_{\bar{x}}$ is the number of samples N.

Defining a fixed sample number for every sampling cycle would be another possibility for algorithm C. Selecting the transmission of N instead of the its definition lead to a higher modularity and an easier adoption of later improvements. Nevertheless this algorithm still has its drawback of a possible overflow, requiring a special treatment.

3.1.2. Transfer

The polled sensor data of one cycle are stored in the probe's memory card and are then transmitted to the surface unit via the Ethernet modem. After receiving this raw data on the TCP server (figure: 3.4) a data backup is stored at the physical storage immediately. Until this point all data remain in their original binary format from now on referred as level zero data.
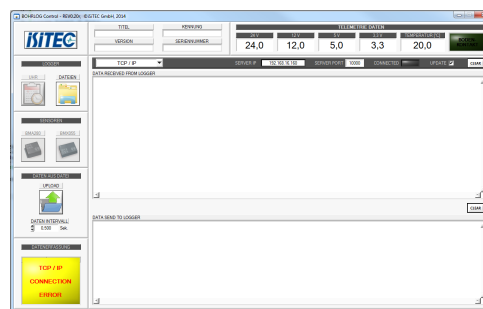
Figure 3.4. Screen-shot of the TCP receiver distributing level zero data.

Shortly after this file output, the latest measurement data are decoded and then are send as a UDP broadcast message on the network stack.

The electronic supplier was contracted for the development and implementation of the firmware for the sensor, bus and main acquisition controller as well as the receiver module.

Considerations of the electronic developer were taken into account leading to the actual design.

3.2. Data transformation and visualisation

The datagram send by the TCP receiver contains a decoded message. It is a multi-line string of characters sorted by the bus address of the sensor. A typical data line referring to an accelerometer has the format:

```
address; status; N_x; sum_x; sq_sum_x; N_y; sum_y; sq_sum_y; N_z; sum_z; sq_sum_z
```

The abbreviation `N`, `sum`, `sq_sum` refer to the values of the statistical analysis where `N` is the number of measurements, `sum` the result of the summed samples and `sq_sum` the sum of the sample squares. This raw data has to be transformed to their corresponding physical parameters. Other static characteristics of the probe which are necessary to perform the transformation are stored in a configuration file. The results of this process are parameters of a certain level defined in the following structure:

- Level zero data

   Receiving raw binary data.

- Level one data

  1. Binary conversion into text-based format.
  2. Sorting addressed data to their related sensors.
  3. Calculation of the mean and the *standard error of the mean.*
  4. Conversion into SI units.

- Level two data

   Calculation of derived parameters.

- Level three data

   Interpretation of the derived parameters.

Data of the same level get stored in individual log files combined with the initial configuration file. Therefore every step of this sequence can be redone with or without later adjustments. It also improves the readability and importing characteristic by reducing the content of each file. Apart from the level zero binary data generated by the TCP receiver (figure: 3.4) all log files are formatted as comma separated value ASCII files. This format can be imported by a wide variety of programs for a further analysis.

All conversions, calculations and transformations get performed by a single C program, which exports its results to the corresponding log file as well as a UDP datagram for the optional visualisation.

The level one data is the first readable data format containing the ordered and converted values and standard deviation of each sensor. This step requires the knowledge of the configured sensor sensitivity, its position and related address.

3.2.1. Level two data

The next level contains data which are not measured directly but are derived from the level one data. Members are density, compass heading, inclination and the contact points. This section focuses on the calculation related to the inclination and geometry of each respective arm. The implemented algorithms for vector rotation or coordinate transformations rely on quaternions. The basic description and definition of this type of number system can be found in appendix D.

The tilt compensation of the compass signal has to be introduced due to the expected high magnetic inclination. This angle describes the direction of the earth magnetic field in respect to the horizon.

The compass heading of an assumed magnetic field vector $\vec{B}$ in a x-y coordinate frame reduces to the calculation of its direction, expressed as the angle between $\vec{B}$ and the x-axes. This angle can be calculated by equation 3.4:

$$\text{heading} = \text{atan2}(y, x) \tag{3.4}$$

The mentioned function atan2 is included in all major programming languages and is defined as the arctangent function with two inputs. In contrast to the *normal* arctangent function with results ranging from $\pm \pi/2$, the two input arctangent function determines the resulting angle over a full circle. The result can be within the interval $\pm \pi$ with a positive sign for counter-clockwise angles.

A three-dimensional sensor always requires a reference plane to perform this angle calculation. The simplest solution would be to define a plane in the sensor coordinate frame and use the projected components of the magnetic field vector as inputs for function 3.4. This approach is reasonable if the defined plane never changes its orientation.

Measuring the change in orientation of the borehole contradicts this simple assumption, therefore a different plane, fixed at the horizon has to be used. The gravity vector is the normal vector of the horizontal plane. When assuming an identical coordinate system for the accelerometer and the magnetometer the changing direction of the acceleration vector can be used to rotate the magnetic field vector back into the global reference frame. As shown in appendix D relates the determination of the rotation axis and angle, to the creation of a single quaternion (equations: D.3 - D.9) and a rotation of vector to a quaternion multiplication (equation D.15).

The rotated x and y components of $\vec{B}$ can be used as inputs for 3.4 to calculate the tilt compensated heading. But this approach assumes an horizontal component of the magnetic field vector. A more accurate estimation requires a model of the local earth's magnetic field.

The distance to a contact point can be calculated by a measurement of the arm angle (ξ). The left case of figure 3.5 shows the fundamental parameters. The distance to the contact point r_{contact} can be calculated by adding the three distances l_{joint}, l_{cont} and the x component l_{arm}:

$$r_{\text{contact}} = l_{\text{joint}} + l_{\text{cont}} + l_{\text{arm}} \sin \xi \tag{3.5}$$

The gravitational acceleration vector (g) measured by the accelerometers located in the probe and in the arm has to be equal even if the probe and arm become laterally disturbed.
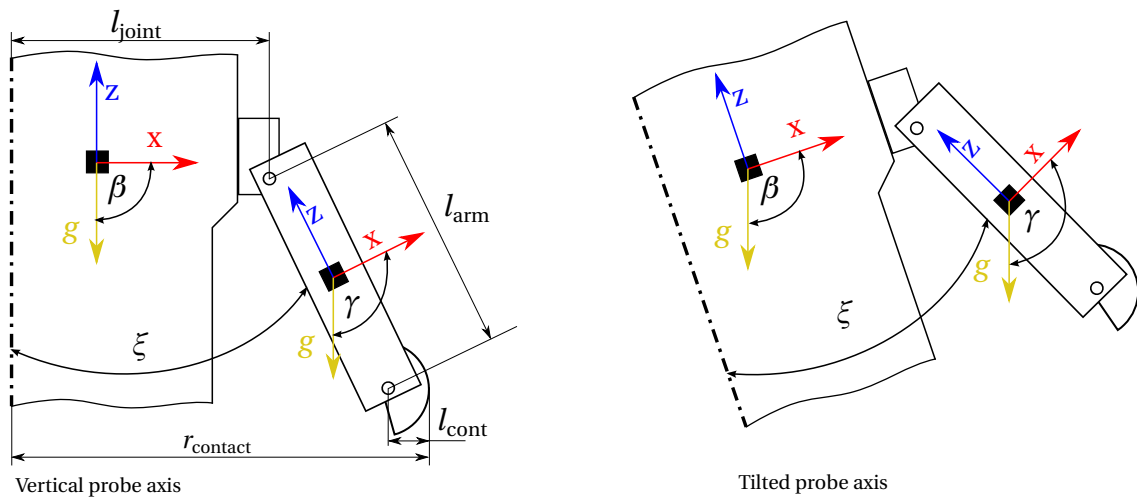
Figure 3.5. Comparison of the contact point measurement, with and without tilt.

The arm angle defined between the two z-axes of the accelerometers results from subtracting the acceleration angles (β and γ). The angle β refers to the reference sensor whereas γ relates to the arm.

$$\xi = \gamma - \beta \tag{3.6}$$

This relation does not change by tilting the probe around the y-axis shown on the right side of figure 3.5. Rotating around the x-axis decreases the vector component within the x-z plane, resulting in a decreasing accuracy of the measured angle. This effect is negligible at small tilt angles but grows until a singularity if the acceleration signal aligns with the y-axis. Therefore a special treatment for this case is needed to prevent the log from arbitrary results.

Transforming the contact point distance to the body fixed coordinate system requires the direction information of each individual arm. In this first iteration this direction vector is given in the configuration file. Detecting this direction automatically is possible for higher tilt angles. By rotating the probe in a dedicated calibration run before each logging operation could be a solution for a higher accuracy in later iterations. In the current step focusing on the prove of functionality, reduces the given information the overall program complexity.

To achieve a full transformation of the contact point position into the local coordinate frame requires the z coordinates of the joint and the calculation of the z component of the arm following a similar trigonometric approach.

The direction vector of the borehole is related to the rotation angle and its axis of the accelerometer calculated for the tilt compensation. In case of a perfect aligned probe the azimuth and inclination angles could be calculated from the already existing quaternion of the gravity vector. Referring to chapter 1.2 a centring mechanism will be added in the future to guarantee a good alignment. Nevertheless, a possible deviation can be measured by adding all local contact points of each ring and calculate the angle (α) shown in figure 1.7. In all cases a plausibility check has to be done due to the measurement of a combined acceleration signal.

Transforming contact points to global coordinates is implemented by the combined rotation of the tilt and the heading. The referring coordinate frame of the resulting point cloud is defined as an x-axis pointing north and a z-axis pointing towards zenith. Combining the point cloud of two or more measurements requires a further post-processing of the depth and information of the initial reference height as well as geographical coordinates. This information can be stored in the configuration file at start of a measurement.

3.2.2. Level three data

All further interpretations of the logged data are summarised as level three data. Most of this analysis are done in the post-processing and are not covered in this thesis. Nevertheless calculation of a regression ellipse of the contact points is implemented in the translate logger data module. Beside of being an example for the further analysis options measuring intraglacial deformations (Schwerzmann et al. 2006) it is used in the *live* visualisation as the shape of the estimated borehole wall.

The regression ellipse is an interpolation method fitting a geometrical curve, in this case an ellipse, into the measured contact points. The used numerical algorithm, adapted from NLREG 2015, minimises the five parameters centre offset (x_0 and y_0), semi major axis (a), semi minor axis (b) and tilt angle (φ) shown in figure 1.11. The key function of this method is the polar equation (3.7) for an ellipse. There ϑ is used as the polar angle as control variable and r the represents the resulting radius.

$$r_{(\vartheta)} = \sqrt{\frac{a^2 b^2}{(a \sin \vartheta)^2 + (b \cos \vartheta)^2}} \tag{3.7}$$

The characterising feature of the resulting ellipse is the aligned semi major axis direction with the x-axis of the coordinate system. Therefore a separate rotation has to be done. The following algorithm is adapted from NLREG 2015:

1. Initial guess of all parameters.

2. Compute the polar angle and distance from the current point relative to the estimated centre.

3. Rotate the polar angle in respect to the ellipse tilt angle $\vartheta = $ polar angle $- \varphi$.

4. Compute the radius of the ellipse for this data angle (equation 3.7).

5. Compute the difference between the distance for the data point and the ellipse.

6. Sum all squared differences of every point.

7. Minimise this deviation sum.

The selected minimising algorithm is based on a star search method in five dimensions (Bullerschen 2009). This rather slow method was selected due to its ease in implementation and the not required calculation of derivatives.

3.2.3. Visualisation

The purpose of the data visualisation is to display essential values in a graphical user interface. The importance of such an interface may not be obvious due to the fact, that it is optional to use and all incoming data are streamed as text also. This text messages contain more than 30 mostly three-axial information, which are hard to read and understand during the operation. Therefore important information is filtered for the visualisation showing the current state of the probe and as far as possible of the borehole. Another reason is the test and debugging phase, requiring a fast access to the basic parameters.

In addition to the pure visualisation this interface should be used to interact with the probe. Examples are the creation of the configuration file before the logging operation starts, resetting of the cable length encoder or the setting of markers to the log file useful for the synchronisation of the paper based log and the digital data. Figure 3.6 shows the user interface with arbitrary data, due to the lack of actual sensor data. The design was selected by the authors taste, and can be changed if necessary. A more basic command-line interface is also available.
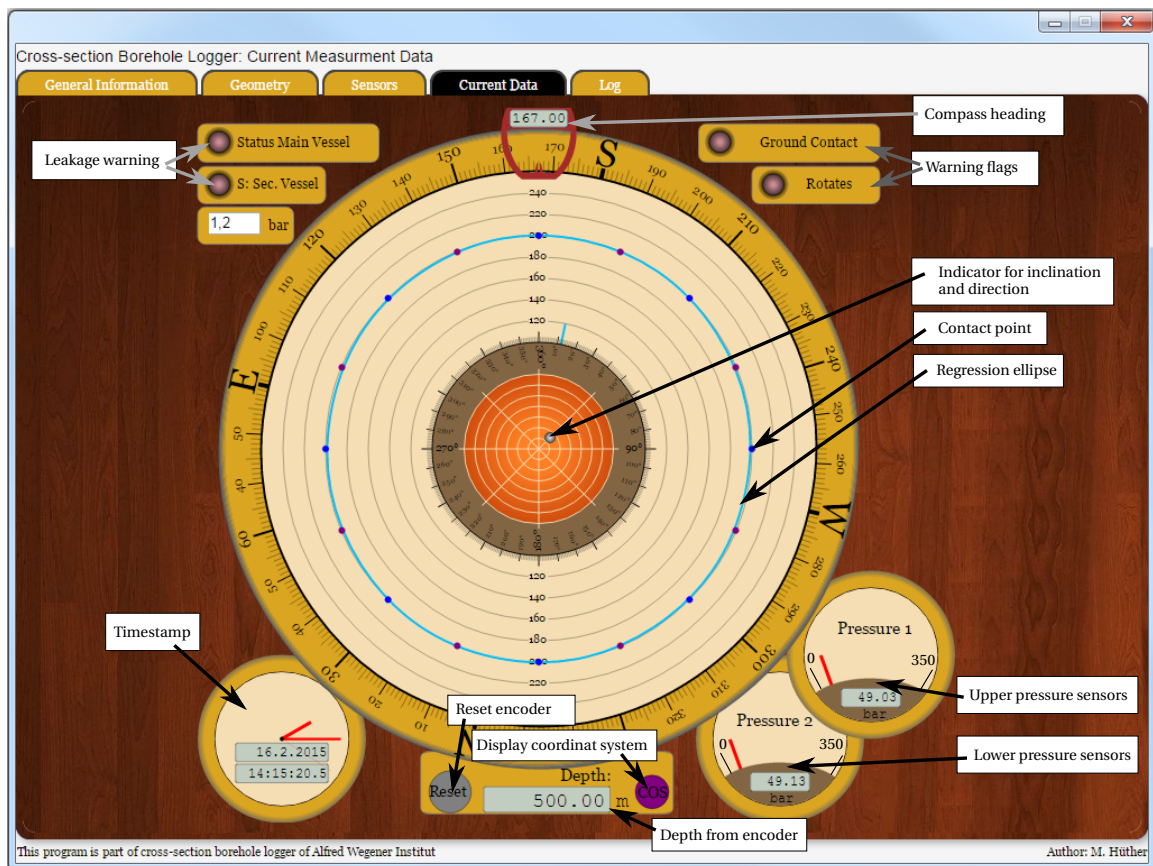

Figure 3.6. Screen-shot of the data visualization. Shown data are arbitrary, due to the lack of actual sensor data.

4. Conclusion

The electronic and software design phase expires with a partial delivery of components and some minor functionality tests. The overall system design seems to fulfil the requirements on data acquisition and handling of 27 three-axial and 10 scalar sensors.

The developed geometry and inclination measurement-system consists of a highly modular 12 port RS-485 bus driven main acquisition board located in a pressure tight sealed housing. All sensors are controlled by their own micro-controller allowing a simple plug-in operation. In addition to the interchangeability of the sensors and their drivers, these controllers evaluate the gathered data in every measurement cycle. The selected algorithm performs a statistical analysis calculating the arithmetic mean of the value combined with standard error of this mean from multiple samples.

The base sensor technology of the 25 accelerometers, one gyroscope and a single magnetometer are microelectromechanical systems. This technology and the amount of sensors are unusual in the field of borehole logging with their extreme environmental conditions of high pressure, low temperature and high chemical reactivity. The main advantages of this class of sensor are the small size and their already implemented amplification and digitalisation modules.

Data rates on the towing cable in the order of high kbit/s and low Mbit/s got recently available, allowing a data synchronisation between surface station and probe during operation. This possibility opens a wide range of data analysis and visualisation.

Next steps are the full integration of all components, followed by a test and calibration sequence. The current early firmware needs to reach production stage and has then to be tested as well. In case of proving their functionality all sensors located outside of the protective electronic compartment requires a mould of epoxy to gain a cover against the harsh environment, before the probe could be immersed in drill liquid for the first time.

Further steps are the construction of a centring mechanism and its implementation. As well as the construction of a pressure housing for the Ethernet modem.

After this test a final system integration phase field tests can be undertaken and additional sensors like the thermometer could be designed for implementation. The following application phase requires sensibility for further improvements and a feedback channel for the engineering group.

The acquired data needs to be analysed by a more sophisticated post-processing chain, which needs to be developed or/and adapted from existing software by the scientific users.

Bibliography

ANSI/TIA/EIA-422-B-1994. Telecommunications Industry Association. URL: `http://rbsfm. org/Downloads/APPNOTE/RS232-485/TIA-EIA422B%20Overview.pdf`.

ANSI/TIA/EIA-485-A-98. Telecommunications Industry Association. URL: `http://joseapicon. com.ve/descargas/componentes/AppNotes759_National.pdf`.

Barlow, R. J. (1989). *Statistics: A Guide to the Use of Statistical Methods in the Physical Sciences.* Manchester Physics Series. Wiley.

Bassler, KH. and H. Miller (1988). 'Evaluation of Hot Water Drills'. In: *Ice Core Drilling. Proceedings of the Third International Workshop on Ice Drilling Technology (eds C. Rado and D. Beaudoing)*, pp. 116–122. URL: `http://www.icedrill.org/Documents/Download. pm?DOCUMENT_ID=786`.

Benn, D.I. and D.J.A. Evans (2010). *Glaciers and Glaciation.* 2nd ed. A Hodder Arnold Publication. Hodder Education. ISBN: 9780340905791.

BMA280: Data sheet (2013). 1.7. Bosch Sensortec.

Bullerschen, K. G. (2009). *Mathematische Optimierung - Script.* FH Aachen.

CAN Specification (1991). URL: `http://esd.cs.ucr.edu/webres/can20.pdf`.

Chabot, Nancy L., Carolyn M. Ernst, Brett W. Denevi, Hari Nair, Ariel N. Deutsch, David T. Blewett, Scott L. Murchie, Gregory A. Neumann, Erwan Mazarico, David A. Paige, John K. Harmon, James W. Head and Sean C. Solomon (2014). 'Images of surface volatiles in Mercury's polar craters acquired by the MESSENGER spacecraft'. In: *Geology*. DOI: `10.1130/G35916.1`.

Colaprete, Anthony, Peter Schultz, Jennifer Heldmann, Diane Wooden, Mark Shirley, Kimberly Ennico, Brendan Hermalyn, William Marshall, Antonio Ricco, Richard C. Elphic, David Goldstein, Dustin Summy, Gwendolyn D. Bart, Erik Asphaug, Don Korycansky, David Landis and Luke Sollitt (2010). 'Detection of Water in the LCROSS Ejecta Plume'. In: *Science* 330.6003, pp. 463–468. DOI: `10.1126/science.1186986`.

Dachwald, B., J. Mikucki, S. Tulaczyk, I. Digel, C. Espe, M. Feldmann, G. Francke, J. Kowalski and C. Xu (2014). 'IceMole: a maneuverable probe for clean in situ analysis and sampling of subsurface ice and subglacial aquatic ecosystems'. In: *Annals of Glaciology* 55.65, pp. 14–22. DOI: `10.3189/2014AoG65A004`.

Francke, G. (2011). 'Designstudie einer Querschnittmesseinrichtung von Bohrlöchern'. German. Not published.

– (2012). 'Fehleranalyse einer Eiskernbohrloch-Querschnittmesseinrichtung unter Labor- und Eislaborbedingungen'. German. Not published.

Gillet, F (1975). 'Steam, hot-water and electrical thermal drills for temperate glaciers'. In: *Journal of Glaciology* 14.70, pp. 171–179.

Großekatthoefer, K and Z. Yoon (2012). *Introduction into quaternions for spacecraft attitude representation.* TU Berlin. URL: `http://www.tu-berlin.de/fileadmin/fg169/ miscellaneous/Quaternions.pdf`.

Grundestrup, N.S., H.B. Clausen and B.L. Hansen (1994). 'The UCPH Borehole Logger'. Englisch. In: *Memoirs of National Institute of Polar Research* 49 (Special Issue No. 49), pp. 224–233. URL: `http://ci.nii.ac.jp/els/110000010330.pdf?id=ART0000331818&type=pdf&lang=en&host=cinii&order_no=&ppv_type=0&lang_sw=&no=1361759143&cp=` (visited on 25/02/2013).

Hambrey, Michael J., Tavi Murray, Neil F. Glasser, Alun Hubbard, Bryn Hubbard, Graham Stuart, Siri Hansen and Jack Kohler (2005). 'Structure and changing dynamics of a polythermal valley glacier on a centennial timescale: Midre Lovénbreen, Svalbard'. In: *Journal of Geophysical Research: Earth Surface* 110.F1. ISSN: 2156-2202. DOI: `10.1029/2004JF000128`.

Harper, J.T., N. F. Humphrey, Pfeffer W. T., D. B. Huzurbazar S. V. Bahr and B. C. Welch (2001). 'Spatial variability in the flow of a valley glacier: Deformation of a large array of boreholes'. In: *Journal of Geophysical Research* 106.B5, pp. 8547–8562.

Head, J. W., D. R. Marchant, M. C. Agnew, C. I. Fassett and M. A. Kreslavsky (2006). 'Extensive valley glacier deposits in the northern mid-latitudes of Mars: Evidence for Late Amazonian obliquity-driven climate change'. In: *Earth and Planetary Science Letters* 241 (3), pp. 663–671. DOI: `10.1016/j.epsl.2005.11.016`.

Hüther, M. (2012). 'Studie einer Messsonde zur Vermessung von Eiskernbohrlöchern'. German. Not published.

– (2013). 'Konstruktion einer Eiskernbohrloch-Querschnittmessvorrichtung'. German. Not published.

John (2011). *MEMS Accelerometer*. InstrumentationToday Webnesters Pvt.Ltd. URL: `http://www.instrumentationtoday.com/mems-accelerometer/2011/08/` (visited on 05/01/2015).

Johnsen, SJ., SB. Hansen, S. Sheldon, G. Simon, D. Dahl-Jensen, JP. Steffensen, L. Augustin, P. Journe, O. Alemany, H. Rufli, J. Schwander, N. Azuma, H. Motoyama, T. Popp, P. Talalay, T. Thorsteinsson, F. Wilhelms and V. Zagorodnov (2007). 'The Hans Tausen drill: design, performance, further developments and some lessons learned'. In: *Annals of Glaciology* 47, pp. 89–98. DOI: `10.3189/172756407786857686`.

Koci, B. R. (1984). 'A Lightweight Hand Coring Auger'. In: *Proceedings of the Second International Workshop/Symposium on Ice Drilling Technology (eds G. Holdsworth, K.C. Kuivinen and J.H. Rand), CRREL Special Report 84-34*, pp. 55–59.

Lefebvre, E., L. Augustin and M. Maitre (2002). 'The EPICA borehole logger'. Englisch. In: *Memoirs of National Institute of Polar Research* 56 (Special Issue No. 56), pp. 264–274. URL: `http://ci.nii.ac.jp/els/110000010513.pdf?id=ART0000332039&type=pdf&lang=en&host=cinii&order_no=&ppv_type=0&lang_sw=&no=1361752730&cp=` (visited on 25/02/2013).

Mashen (2013). *File:Quaternion 2.svg*. Wikimedia Commons. URL: `https://commons.wikimedia.org/wiki/File:Quaternion_2.svg` (visited on 26/01/2015).

NASA (2005). *Mass balance atmospheric circulation*. Wikimedia Commons. URL: `http://en.wikipedia.org/wiki/Image:Mass_balance_atmospheric_circulation.png` (visited on 15/12/2014).

NLREG (2015). *Elliptical Regression – Fit an Ellipse to Data Points*. URL: `http://www.nlreg.com/ellipse.htm` (visited on 01/02/2015).

Philberth, K. (1972). 'Wired Probe for Measuring the Temperature Profile on Icecaps'. In: *Cold Regions Research and Engineering Laboratoy TL 373*. URL: `http://www.icedrill.org/Documents/Download.pm?DOCUMENT_ID=333`.

Postel, J. (1980). *Request for Comments 768: User Datagram Protocol.* The Internet Engineering Task Force (IETF). URL: https://tools.ietf.org/html/rfc768 (visited on 26/01/2015).

Princeton.edu (2007). *MEMS/Nanoscale Thin Films.* The Trustees of Princeton University - The Department of Mechanical and Aerospace Engineering. URL: http://www.princeton.edu/mae/people/faculty/soboyejo/research_group/images/mems.png (visited on 05/01/2015).

Prockter, Louise M. (2005). 'Ice in the Solar System'. In: *Johns Hopkins APL Technical Digest* 26.2, pp. 175–188. URL: http://www.jhuapl.edu/techdigest/TD/td2602/Prockter.pdf.

Schwerzmann, A., M. Funk and H. Blatter (2006). 'Instruments and Methods Borehole logging with an eight-arm caliper–inclinometer probe'. Englisch. In: *Journal of Glaciology* 52.178, pp. 381–388. URL: http://www.iac.ethz.ch/doc/publications/j05J024.pdf (visited on 23/02/2013).

Southern California, University of (1981). *Request for Comments 793: Transmission Control Protocol.* Defense Advanced Research Projects Agency (DARPA). URL: https://tools.ietf.org/html/rfc793 (visited on 26/01/2015).

Talalay, P.G. and N.S. Grundestrup (2002). 'Hole fluids for deep ice core drilling'. Englisch. In: *Memoirs of National Institute of Polar Research* Special Issue No. 56: *Ice Drilling Technology 2000*, pp. 148–170.

Nomenclature

α Deviation angle between the probe alignment and the borehole axis

$\bar{x}$ Arithmetic mean

$\sigma_{\bar{x}}$ Standard error of the mean

θ Transformation angle

ε_0 Electric constant

ε_r Relative static permittivity

φ Tilt angle of the ellipse

ϑ Polar angle

$\vec{a}$ Acceleration

$\vec{B}$ Magnetic filed vector

$\vec{F}_a$ Force due to acceleration

$\vec{F}_s$ Force of a spring

$\vec{x}$ Spring deformation

ξ Arm angle

A Area

a Semi major axis

b Semi minor axis

C Capacitance

d Distance

k Spring constant

l Length

m Mass

N Number of measurements

q_s Real factor of a quaternion

q_x Factor of the quaternion element i

q_y Factor of the quaternion element j

q_z Factor of the quaternion element k

$q_{B \leftarrow A}$ Coordinate transformation from a vector in system A to B

r Radius

x_0 X coordinate of the ellipse center

x_i Value of a single measurement

y_0 Y coordinate of the ellipse center

g   Gravitational acceleration vector

Glossary

CAN-BUS is a vehicle bus standard designed to allow micro controllers and devices to communicate with each other without a single master. The protocol is message based and supports prioritisation which is required by hard real time systems. 19, 20

Ethernet is a family of computer networking technologies for local area networks. 20–23, 27, 33

I²C Inter-Integrated Circuit is a multi-master, multi-slave, single-ended, serial computer bus. Its application field are low-speed peripherals communicating to motherboards and embedded systems. 19

RS-232 is a standard for serial communication transmission of data. The RS-232 standard is commonly used in computer serial ports. 19, 20

RS-422 specifies electrical characteristics of a digital signalling circuit. It refers to the standard *ANSI/TIA/EIA-422-B-1994* n.d.. 19, 20

RS-485 is a standard defining the electrical characteristics of drivers and receivers for use in balanced digital multipoint systems. 19–24, 33

RTC Real time clocks are used in hardware to determine the current time. They require a independent power supply. 21

SPI Serial peripheral interface bus, is a synchronous serial communications device used for short distance, single master communication. 19

TCP Transmission Control Protocol, is a network protocol formally defined in RFC 768 (Southern California 1981). TCP provides reliable, ordered and error-checked delivery of a stream of octets between programs running on computers connected to a local area network. It is the underlying protocol of typical web protocols like HTTP or email. 23, 27, 28

UDP The User Datagram Protocol, is a network protocol formally defined in RFC 768 (Postel 1980). It uses a connectionless transmission model with no handshake and error correction algorithm, but provides checksums for data integrity. Therefore it is typically used in time-sensitive applications which prefer dropped over delayed packages. 23, 27, 28

USB Universal serial bus is a defined industry standard for computer peripherals. It include the hardware level (cable and connectors) as well as the protocol. The ubiquitous application result in a good support of every major operation system and cheep hardware. 20–22, 24

List of figures

List of tables

Appendices

A. MEMS accelerometer

The required measurement of the distance change can be further improvement by adding a second capacitor below the rib. This two capacitors are labelled with C_1 and C_2 in figure 1.8. In the case of a upward displacement of the proof mass the distance (d_1) of C_1 increases resulting in a lower capacitance. At the same time the reverse sequence happens at C_2.

$$0 \; = \; (V_x + V_0)C_1 + (V_x - V_0)C_2 \tag{A.1}$$

$$0 \; = \; V_x(C_1 + C_2) + V_0(C_1 - C_2) \tag{A.2}$$

$$V_x \; = \; V_0\left(\frac{C_2 - C1}{C_1 + C_2}\right) \tag{A.3}$$

with the assumption $A_1 = A_2$

$$C_1 = \varepsilon_r \varepsilon_0 \frac{A}{d_1} \tag{A.4}$$

$$C_2 = \varepsilon_r \varepsilon_0 \frac{A}{d_2} \tag{A.5}$$

Set equations A.4 and A.5 in A.3

$$V_x \; = \; V_0\left(\frac{\varepsilon_r \varepsilon_0 \frac{A}{d_2} - \varepsilon_r \varepsilon_0 \frac{A}{d_1}}{\varepsilon_r \varepsilon_0 \frac{A}{d_1} + \varepsilon_r \varepsilon_0 \frac{A}{d_2}}\right) \tag{A.6}$$

$$V_x \; = \; V_0\left(\frac{\frac{1}{d_2} - \frac{1}{d_1}}{\frac{1}{d_1} + \frac{1}{d_2}}\right) \tag{A.7}$$

$$V_x \; = \; V_0\left(\frac{\frac{d_1 - d_2}{d_1 d_2}}{\frac{d_1 + d2}{d_1 d_2}}\right) \tag{A.8}$$

$$V_x \; = \; V_0\left(\frac{d_1 - d_2}{d_1 + d2}\right) \tag{A.9}$$

substitute $d_1 = d + x$ and $d_2 = d - x$ in A.9

$$V_x = V_0\left(\frac{x}{d}\right) \tag{A.10}$$

Set into equation1.3 results to

$$a_x = -\frac{k d V_x}{m V_0} \tag{A.11}$$

B. Statistic code examples

Pseudo-code: Algorithm for the calculation of $\bar{x}$ and $\sigma_{\bar{x}}^2$

```c
uint8_t  n;                      // 1 byte
uint8_t  i;                      // 1 byte
int16_t  x_i[3];                 // 6 byte
int64_t  x_sq_sum[3];            // 24 byte
int32_t  x_sum[3];               // 12 byte
double   factor;                 // 8 byte
double   x_mean[3];              // 24 byte
double   sigmaSQ[3];             // 24 byte

do {
  for(i=0;i<3;i++){
    x_sum[i] = 0;
    x_sq[i] = 0;
  }
  n = 0;
  do {
    for(i=0;i<3;i++){
      x_sum[i] += x_i[i];
      x_sq_sum[i] += x_i[i] * x_i[i];
    }
    n++;
  } while(!loop); /* As long as values exists */

  factor = 1./(n-1.);
  for(i=0;i<3;i++){
    sigmaSQ[i] = factor * ( (double)x_sq_sum[i] - (double)(x_sum[
        i] * x_sum[i]) / n );
    x_mean[i] = (double)x_sum[i] / n;
  }
  send(x_mean[0], sigmaSQ[0], x_mean[1], sigmaSQ[1], x_mean[2],
      sigmaSQ[2]);
} while(1);
```

Pseudo-code: Algorithm for the calculation of N, $\sum x_i$ und $\sum x_i^2$

```c
uint8_t n;                          // 1 byte
uint8_t i;                          // 1 byte
int16_t x_i[3];                     // 6 byte
int64_t x_sq_sum[3];                // 24 byte
int32_t x_sum[3];                   // 12 byte

do {
  for(i=0;i<3;i++){
    x_sum[i] = 0;
    x_sq[i] = 0;
  }
  n = 0;

  do {
    for(i=0;i<3;i++){
      x_sum[i] += x_i[i];
      x_sq_sum[i] += x_i[i] * x_i[i];
    }
    n++;
  } while(!loop); /* As long as values exists */

  send(n, x_sum[0], x_sq_sum[0], x_sum[1], x_sq_sum[1], x_sum[2],
      x_sq_sum[2]);
} while(1);
```

C. Basic functions of linear algebra

Implemented functions for three dimensional vector:

```c
typedef double vec3[3];
extern void vec3_add(vec3 r, vec3 a, vec3 b){
    int i;
    for(i=0; i<3; ++i)
        r[i] = a[i] + b[i];
}
extern void vec3_sub(vec3 r, vec3 a, vec3 b){
    int i;
    for(i=0; i<3; ++i)
        r[i] = a[i] - b[i];
}
extern void vec3_scale(vec3 r, vec3 v, double s){
    int i;
    for(i=0; i<3; ++i)
        r[i] = v[i] * s;
}
extern double vec3_mul_inner(vec3 a, vec3 b){
    double p = 0.;
    int i;
    for(i=0; i<3; ++i)
        p += b[i]*a[i];
    return p;
}
extern void vec3_mul_cross(vec3 r, vec3 a, vec3 b){
    r[0] = a[1]*b[2] - a[2]*b[1];
    r[1] = a[2]*b[0] - a[0]*b[2];
    r[2] = a[0]*b[1] - a[1]*b[0];
}
extern double vec3_len(vec3 v){
    return sqrt(vec3_mul_inner(v, v));
}
extern void vec3_norm(vec3 r, vec3 v){
    vec3_scale(r, v, 1. / vec3_len(v));
    extern void vec4_norm(vec4 r, vec4 v){
        vec4_scale(r, v, 1. / vec4_len(v));
    }
}
```

Implemented functions for four dimensional vector (required for quaternion calculation):

```c
typedef double vec4[4];
extern void vec4_add(vec4 r, vec4 a, vec4 b){
    int i;
    for(i=0; i<4; ++i)
        r[i] = a[i] + b[i];
}
extern void vec4_sub(vec4 r, vec4 a, vec4 b){
    int i;
    for(i=0; i<4; ++i)
        r[i] = a[i] - b[i];
}
extern void vec4_scale(vec4 r, vec4 v, double s){
    int i;
    for(i=0; i<4; ++i)
        r[i] = v[i] * s;
}
extern double vec4_mul_inner(vec4 a, vec4 b){
    double p = 0.;
    int i;
    for(i=0; i<4; ++i)
        p += b[i]*a[i];
    return p;
}
extern void vec4_mul_cross(vec4 r, vec4 a, vec4 b){
    r[0] = a[1]*b[2] - a[2]*b[1];
    r[1] = a[2]*b[0] - a[0]*b[2];
    r[2] = a[0]*b[1] - a[1]*b[0];
    r[3] = 1.;
}
extern double vec4_len(vec4 v){
    return sqrt(vec4_mul_inner(v, v));
}
extern void vec4_norm(vec4 r, vec4 v){
    vec4_scale(r, v, 1. / vec4_len(v));
}
```

D. Quaternions

Quaternions are a hyper-complex number system, consisting of four *dimensions*. They can be understood as the extension of the complex number system. The following description is adapted from Großekatthoefer and Yoon 2012.
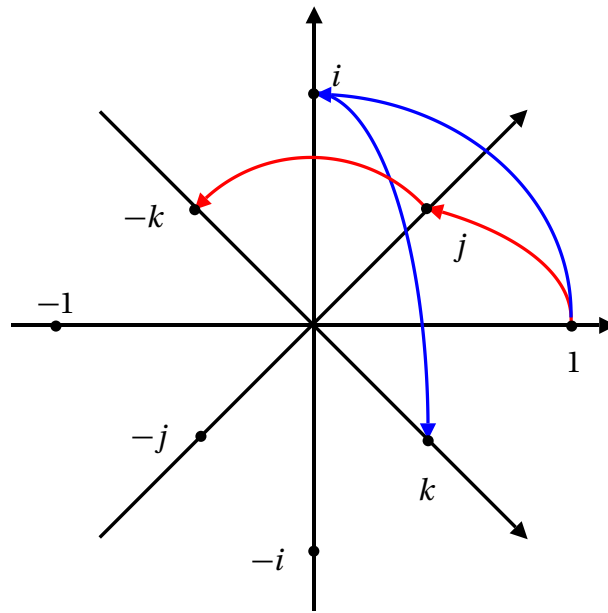
Figure D.1. Graphical representation of quaternion units product as 90° rotation in a four dimensional space. Mashen 2013

The identity of the base elements is:

$$i^2 = j^2 = k^2 = ijk = -1 \tag{D.1}$$

This base element can be written as a linear combination with four elements $q_s 1 + q_x i + q_y j + q_z k$. The literature often expresses only the four factors in a 4×1 matrix with different definitions. In this document following definition is applied. In some cases the factors of i, j and k are summarised as a vector and the factor of the 1 is referenced as the real part.

$$q = \begin{bmatrix} \vec{v} \\ q_s \end{bmatrix} = \begin{bmatrix} q_x \\ q_y \\ q_z \\ q_s \end{bmatrix} \tag{D.2}$$

One important mathematical characteristic is the non-commutative multiplication of two quaternions. Like Euler angles or rotation matrices quaternions are able to express three dimensional rotations. There the direction of $\vec{v}$ corresponds with the rotation axis and the magnitude combined with the real part q_s with the rotation angle (equation D.3). In contrast

to Euler angles, quaternions require one more information but avoid the occurrence of a *gimbal lock*.

The term *gimbal lock* refers phenomena found in a set of three gimbals. This singularity appears in the case of a pitch angle of 90°. Then changes yaw and roll angle reduces to the axis and rotations around the initial roll axis are blocked.

This singularity can be prevented also by using rotation matrices, which are 3×3 matrices containing six different factors due to their symmetry. Therefore quaternions are numerically lighter but their physical interpretation is much more complex. The numerical characteristic leads to their common application in computational graphics, analysis and in guidance-navigation and control applications.

A coordinate transformation from a vector in system A to B ($q_{B \leftarrow A}$) can be calculated by equation D.3. There $\|\vec{e}\|$ refers to normalized rotation axis and θ to the transformation angle.

$$q_{B \leftarrow A} = \begin{bmatrix} \|\vec{e}\| \sin\left(\frac{\theta}{2}\right) \\ \cos\left(\frac{\theta}{2}\right) \end{bmatrix} \tag{D.3}$$

The rotation axis can be calculated through the cross product.

$$\|\vec{e}\| = \frac{\vec{a} \times \vec{b}}{|\vec{a} \times \vec{b}|} \tag{D.4}$$

For implementing this in to an algorithm it is preferable to prevent the usage of trigonometrical functions due to there approximation algorithms. Therefore it was implemented as follows:

The sine of a half angle can be rewritten in:

$$\sin\left(\frac{\theta}{2}\right) = \pm\sqrt{\frac{1 - \cos\theta}{2}} \tag{D.5}$$

and the cosine half angle:

$$\cos\left(\frac{\theta}{2}\right) = \pm\sqrt{\frac{1 + \cos\theta}{2}} \tag{D.6}$$

Using the definition of the scalar product

$$\vec{a} \circ \vec{b} = |\vec{a}||\vec{b}| \cos\theta \tag{D.7}$$

the cosine can be rewritten to:

$$\cos\theta = \frac{\vec{a} \circ \vec{b}}{|\vec{a}||\vec{b}|} \tag{D.8}$$

Now the quaternion can be rewritten to:

$$q_{B \leftarrow A} = \pm\begin{bmatrix} \sqrt{\frac{1 - \cos\theta}{2}} \|\vec{e}\| \\ \sqrt{\frac{1 + \cos\theta}{2}} \end{bmatrix} = \pm\begin{bmatrix} \sqrt{\frac{1 - \frac{\vec{a} \circ \vec{b}}{|\vec{a}||\vec{b}|}}{2}} \frac{\vec{a} \times \vec{b}}{|\vec{a} \times \vec{b}|} \\ \sqrt{\frac{1 + \frac{\vec{a} \circ \vec{b}}{|\vec{a}||\vec{b}|}}{2}} \end{bmatrix} \tag{D.9}$$

with $\cos\theta$ from equation: D.8 and $\|\vec{e}\|$ from equation: D.4. The sign in front of the square root is define either it to a coordinate transformation or a rotation.

Quaternion mathematics

Norm

$$|q| = \sqrt{q_s^2 + q_x^2 + q_y^2 + q_z^2} \tag{D.10}$$

Normalization

$$\|q\| = \frac{q}{|q|} \tag{D.11}$$

Conjugate

$$q^* = \begin{bmatrix} -q_x \\ -q_y \\ -q_z \\ q_s \end{bmatrix} \tag{D.12}$$

Inverse

$$q^{-1} = \frac{q^*}{|q|} \tag{D.13}$$

Multiplication

$$q_1 \otimes q_2 = q = \begin{bmatrix} \vec{v} \\ s \end{bmatrix} = \begin{bmatrix} s_1 \vec{v}_2 + s_2 \vec{v}_1 + \vec{v}_1 \times \vec{v}_2 \\ s_1 s_2 - \vec{v}_1 \circ \vec{v}_2 \end{bmatrix} \tag{D.14}$$

Transformation

The transformation of $\vec{v}$ from A to B is defined by:

$$\vec{v}_B = q_{B \leftarrow A} \otimes \begin{bmatrix} \vec{v}_A \\ 0 \end{bmatrix} \otimes q_{B \leftarrow A}^{-1} \tag{D.15}$$

Implementation

```
typedef double quat[4];
extern void quat_identity(quat q){
    q[0] = q[1] = q[2] = 0.;
    q[3] = 1.;
}
extern void quat_add(quat r, quat a, quat b){
    int i;
    for(i=0; i<4; ++i)
        r[i] = a[i] + b[i];
}
extern void quat_sub(quat r, quat a, quat b){
    int i;
    for(i=0; i<4; ++i)
        r[i] = a[i] - b[i];
}
extern void quat_mul(quat r, quat p, quat q){
    vec3 w;
    vec3_mul_cross(r, p, q);
    vec3_scale(w, p, q[3]);
    vec3_add(r, r, w);
    vec3_scale(w, q, p[3]);
    vec3_add(r, r, w);
    r[3] = p[3]*q[3] - vec3_mul_inner(p, q);
}
extern void quat_scale(quat r, quat v, double s){
    int i;
    for(i=0; i<4; ++i)
        r[i] = v[i] * s;
}
extern double quat_inner_product(quat a, quat b){
    double p = 0.;
    int i;
    for(i=0; i<4; ++i)
        p += b[i]*a[i];
    return p;
}
extern void quat_conj(quat r, quat q){
    int i;
    for(i=0; i<3; ++i)
        r[i] = -q[i];
    r[3] = q[3];
}
#define quat_norm vec4_norm

extern void quat_mul_vec3(vec3 r, quat q, vec3 v){
    quat v_ = {v[0], v[1], v[2], 0.};

    quat_conj(r, q);
    quat_norm(r, r);
    quat_mul(r, v_, r);
    quat_mul(r, q, r);
}
```

```c
extern void RotQuat_between_vectors(quat q, vec3 a, vec3 b){
    double cosAngle, rootFactor;
    vec3 rotAxis;

    cosAngle = vec3_mul_inner(a, b) /( vec3_len(a) * vec3_len(b)
        );

/* If cos(angle) = 1 there is no rotation */
    if(1.-abs(cosAngle) < 1e-6){
        q[0] = 0;
        q[1] = 0;
        q[2] = 0;
        q[3] = 1;
    }
    else{
        vec3_mul_cross(rotAxis, a, b);
        vec3_norm(rotAxis, rotAxis);
        rootFactor = sqrt( 0.5 * ( 1 - cosAngle) );

        q[0] = rootFactor * rotAxis[0];
        q[1] = rootFactor * rotAxis[1];
        q[2] = rootFactor * rotAxis[2];
        q[3] = sqrt( 0.5 * (1 + cosAngle) );
    }
}
```

This implementation works only in conjunction with the implemented function of linear algebra in appendix C.

E. Surface unit applications

Structure

```
└─ Isitec/
   ├─ BOHRLOGGER/
   ├─ SENSOR TEST GUI/
   ├─ AVR_Bootloader/
└─ GeometryLoggerControl/
   ├─ appData/
   │  └─ config
   ├─ css/
   │  ├─ main.css
   │  ├─ meta.css
   ├─ html/
   │  └─ index.html
   ├─ jquery/
   │  └─ jquery.min.js
   ├─ js/
   │  ├─ background.js
   │  ├─ common.js
   │  ├─ config.js
   │  ├─ current.js
   │  ├─ main.js
   ├─ pics/
   │  ├─ logo-16.png
   │  ├─ logo-128.png
   │  ├─ wood_texture.jpg
   ├─ manifest.json
   └─ ...

└─ GeometryBohrlochLogger/
   ├─ appData/
   │  └─ config
   ├─ bin/
   │  ├─ sendUDP_MC_Encoder.exe
   │  ├─ TGLF.exe
   │  ├─ UDPControl.exe
   ├─ Encoder/
   │  ├─ Encoder.ino
   ├─ header/
   │  ├─ analysis.h
   │  ├─ cJSON.h
   │  ├─ lmath.h
   │  ├─ serialport.h
   │  ├─ UDPcom.h
   ├─ sendUDP_Encoder/
   │  ├─ makefile
   ├─ source/
   │  ├─ cJSON.c
   │  ├─ sendUDP_Encoder.c
   │  ├─ serialport.c
   │  ├─ TranslateGeometryLoggerFormat.c
   │  ├─ UDPcom.c
   │  ├─ UDPControl.c
   ├─ TGLF/
   │  ├─ makefile
   ├─ UDPControl/
   │  ├─ makefile
   ├─ buildProject.sh
```

Source code

The source code of all programs can be supplied upon request.